Chapter 6
Spatial Joints with Clearance: Dry Contact Models

The problem of the dynamic behavior of planar multibody systems with clearance joints was developed in the previous chapters. The utility of the methodologies developed is somewhat restricted because they are not valid for spatial multibody systems such as vehicle models, car suspensions and robotic manipulators, where the system motion is not limited to be planar. In fact, even planar systems may exhibit out-of-plane motion due to misalignments, thus justifying the development of mathematical models to assess the influence of the clearance joints in spatial multibody systems. The main purpose of this chapter is to present effective methodologies for spatial multibody systems including both the spherical and the revolute joints with clearance. Due to their relevance for this chapter, some aspects of the multibody formulation for spatial systems, based on the Cartesian coordinates, are reviewed here to introduce the basic aspects on the dynamic modeling of spatial multibody systems with clearance joints (Nikravesh 1988). A brief description of the ideal, or perfect, spherical and spatial revolute joints is presented. Similar to the case of planar formulation, the bodies that constitute the spatial clearance joints are modeled as colliding bodies and contact-impact forces control the dynamic behavior of the joint elements. For this purpose, the joint elements are considered as elastic bodies in contact, in which relative penetration exists, but without deformation. The normal contact force that depends on this pseudo-penetration follows the contact-impact force model proposed by Lankarani and Nikravesh (1990). This force model, which is a function of the bodies' relative motion and of the internal geometry of the joint, leads to the contact forces that are introduced in the system's equations of motion. In this methodology, the clearance plays a key role in the joint kinematics. Simple spatial mechanical systems that describe spatial motion, such as the four-bar mechanism and the double pendulum, are used to illustrate the methodologies and assumptions adopted. In addition, a slider–crank mechanism that describes a planar motion is also considered, as an application example, in order to compare both the planar and spatial formulation for clearance joints.

P. Flores et al., *Kinematics and Dynamics of Multibody Systems with Imperfect Joints.*

6.1 Spatial Multibody Systems

This section presents the formulation of the general equations of motion to the spatial dynamic analysis of multibody systems. A simple and brief description of the standard mechanical joints of spatial multibody mechanical systems is presented, namely of the ideal spherical and revolute joints, to emphasize the differences with respect to joints with clearance, introduced later. The methodology presented can be implemented in any general-purpose multibody code, tested in particular in the computer program DAP-3D, which has been developed for the spatial dynamic analysis of general multibody systems (Nikravesh 1988). Due to its simplicity and computational easiness, Cartesian coordinates and Newton–Euler's method are used to formulate the equations of motion of the spatial multibody systems.

Let Fig. 6.1 represent a rigid body i to which a body-fixed coordinate system $(\xi\eta\zeta)_i$ is attached at its center of mass. When Cartesian coordinates are used, the position and orientation of the rigid body must be defined by a set of translational and rotational coordinates. The position of the body with respect to global coordinate system XYZ is defined by the coordinate vector $\mathbf{r}_i = [\,x\ y\ z\,]_i^T$ that represents the location of the local reference frame $(\xi\eta\zeta)_i$. The orientation of the body is described by the rotational coordinate's vector $\mathbf{p}_i = [\,e_0\ e_1\ e_2\ e_3\,]_i^T$, which is made with the Euler parameters for the rigid body (Nikravesh 1988). Therefore the vector of coordinates that completely describes the rigid body i is

$$\mathbf{q}_i = [\,\mathbf{r}_i^T\ \mathbf{p}_i^T\,]_i^T \tag{6.1}$$

A spatial multibody system with *nb* bodies is described by a set of coordinates $\mathbf{q}$ in the form

$$\mathbf{q} = [\mathbf{q}_1^T, \mathbf{q}_2^T, \ldots, \mathbf{q}_{nb}^T]^T \tag{6.2}$$

The location of point P on body i can be defined by the position vector $\mathbf{s}_i^P$ with respect to the body-fixed reference frame $(\xi\eta\zeta)_i$ and by the global position vector $\mathbf{r}_i$, that is,

$$\mathbf{r}_i^P = \mathbf{r}_i + \mathbf{s}_i^P = \mathbf{r}_i + \mathbf{A}_i \mathbf{s}_i'^P \tag{6.3}$$

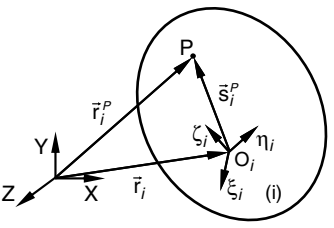

Fig. 6.1 Definition of the Cartesian coordinates for a rigid body

where $\mathbf{A}_i$ is the transformation matrix for body i that defines the orientation of the referential $(\xi\eta\zeta)_i$ with respect to the referential frame XYZ. The transformation matrix is expressed as function of the four Euler parameters as (Nikravesh 1988)

$$\mathbf{A}_i = \begin{bmatrix} e_0^2 + e_1^2 - \frac{1}{2} & e_1e_2 - e_0e_3 & e_1e_3 + e_0e_2 \\ e_1e_2 + e_0e_3 & e_0^2 + e_2^2 - \frac{1}{2} & e_2e_3 - e_0e_1 \\ e_1e_3 - e_0e_2 & e_2e_3 + e_0e_1 & e_0^2 + e_3^2 - \frac{1}{2} \end{bmatrix}_i \tag{6.4}$$

Notice that the vector $\mathbf{s}_i^P$ is expressed in global coordinates whereas the vector $\mathbf{s}_i'^P$ is defined in the body i fixed coordinate system. Throughout the formulation presented in this work, the quantities with $(.)'$ mean that $(.)$ is expressed in local system coordinates.

The velocities and accelerations of body i use the angular velocities $\boldsymbol{\omega}'_i$ and accelerations $\dot{\boldsymbol{\omega}}'_i$ instead of the time derivatives of the Euler parameters, which simplifies the mathematical formulation and does not require the use of mathematical constraint for Euler parameters. The relation between the Euler parameters $\dot{e}_0 + \dot{e}_1 + \dot{e}_2 + \dot{e}_3 = 0$ is implied in the angular velocity and, therefore, is not used explicitly (Nikravesh and Chung 1982). When Euler parameters are employed as rotational coordinates, the relation between their time derivatives, $\dot{\mathbf{p}}_i$, and the angular velocities is expressed by (Nikravesh 1988)

$$\dot{\mathbf{p}}_i = \tfrac{1}{2}\mathbf{L}^T\boldsymbol{\omega}'_i \tag{6.5}$$

where the auxiliary 3×4 matrix $\mathbf{L}$ is a function of Euler parameters (Nikravesh 1988)

$$\mathbf{L}_i = \begin{bmatrix} -e_1 & e_0 & e_3 & -e_2 \\ -e_2 & -e_3 & e_0 & e_1 \\ -e_3 & e_2 & -e_1 & e_0 \end{bmatrix}_i \tag{6.6}$$

The velocities and accelerations of body i are given by vectors

$$\dot{\mathbf{q}}_i = [\,\dot{\mathbf{r}}_i^T \;\; \boldsymbol{\omega}_i'^T\,]_i^T \tag{6.7}$$

$$\ddot{\mathbf{q}}_i = [\,\ddot{\mathbf{r}}_i^T \;\; \dot{\boldsymbol{\omega}}_i'^T\,]_i^T \tag{6.8}$$

In terms of the Cartesian coordinates, the equations of motion of an unconstrained multibody mechanical system are written as

$$\mathbf{M}\ddot{\mathbf{q}} = \mathbf{g} \tag{6.9}$$

where $\mathbf{M}$ is the global mass matrix, containing the mass and moment of inertia of all bodies and $\mathbf{g}$ is a force vector that contains the external and Coriolis forces acting on the bodies of the system.

For a constrained multibody system, the kinematical joints are described by a set of holonomic algebraic constraints denoted as

$$\mathbf{\Phi}(\mathbf{q}, t) = \mathbf{0} \tag{6.10}$$

Using the Lagrange multipliers technique the constraints are added to the equations of motion. These are written together with the second time derivative of the constraint equations. Thus the set of equations that describe the motion of the multibody system is

$$\begin{bmatrix} \mathbf{M} & \mathbf{\Phi}_{\mathbf{q}}^T \\ \mathbf{\Phi}_{\mathbf{q}} & \mathbf{0} \end{bmatrix} \begin{Bmatrix} \ddot{\mathbf{q}} \\ \boldsymbol{\lambda} \end{Bmatrix} = \begin{Bmatrix} \mathbf{g} \\ \boldsymbol{\gamma} \end{Bmatrix} \tag{6.11}$$

where $\boldsymbol{\lambda}$ is the vector of Lagrange multipliers and $\boldsymbol{\gamma}$ is the vector that groups all the terms of the acceleration constraint equations that depend on the velocities only, that is,

$$\boldsymbol{\gamma} = -(\mathbf{\Phi}_{\mathbf{q}}\dot{\mathbf{q}})_{\mathbf{q}}\dot{\mathbf{q}} - \mathbf{\Phi}_{tt} - 2\mathbf{\Phi}_{\mathbf{q}t}\dot{\mathbf{q}} \tag{6.12}$$

The Lagrange multipliers, associated with the kinematic constraints, are physically related to the reaction forces and moments generated between the bodies interconnected by kinematic joints.

Equation (6.11) is a differential algebraic equation that has to be solved, the resulting accelerations being integrated in time. However, in order to avoid constraints violation during numerical integration, the Baumgarte (1972) stabilization technique is used, (6.11) being modified to

$$\begin{bmatrix} \mathbf{M} & \mathbf{\Phi}_{\mathbf{q}}^T \\ \mathbf{\Phi}_{\mathbf{q}} & \mathbf{0} \end{bmatrix} \begin{Bmatrix} \ddot{\mathbf{q}} \\ \boldsymbol{\lambda} \end{Bmatrix} = \begin{Bmatrix} \mathbf{g} \\ \boldsymbol{\gamma} - 2\alpha\dot{\mathbf{\Phi}} - \beta^2\mathbf{\Phi} \end{Bmatrix} \tag{6.13}$$

where α and β are positive constants that represent the feedback control parameters for the velocity and position constraint violations (Baumgarte 1972, Nikravesh 1988). This issue is presented and discussed in detail in Chap. 2, the conclusions being valid for spatial systems also. The same applies to the use of the vector calculus and the numerical methods for planar dynamics of multibody systems presented in previous chapters, which are still adequate for the treatment of spatial systems.

According to the formulation outlined, the dynamic response of multibody systems involves the evaluation of the Jacobian matrix $\mathbf{\Phi}_{\mathbf{q}}$ and vectors $\mathbf{g}$ and $\boldsymbol{\gamma}$, in each time step. The solution of (6.13) is obtained for the system accelerations $\ddot{\mathbf{q}}$. These accelerations, together with the velocities $\dot{\mathbf{q}}^*$, are integrated to obtain the new velocities $\dot{\mathbf{q}}$ and positions $\mathbf{q}^*$ for the next time step. This process is repeated until the complete description of system motion is obtained for a selected time interval. Note that, in vector $\dot{\mathbf{q}}^*$, the angular velocities are substituted by the time derivatives of the Euler parameters using (6.5).

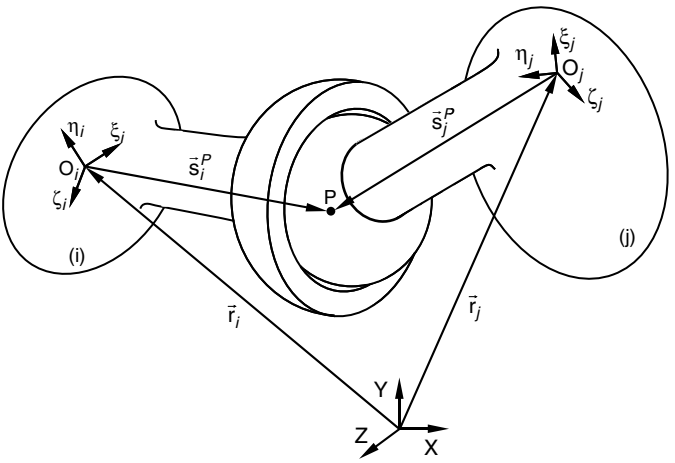

Fig. 6.2 Perfect spherical joint in a multibody system

An ideal or perfect spherical joint, also known as the ball and socket joint, illustrated in Fig. 6.2, constrains the relative translations between two adjacent bodies i and j, allowing only three relative rotations. Therefore the center of the spherical joint, point P, has constant coordinate with respect to any of the local coordinate systems of the connected bodies, i.e., a spherical joint is defined by the condition that the point P_i on body i coincides with the point P_j on body j. This condition is simply the spherical constraint, which can be written in a scalar form as (Nikravesh 1988)

$$\mathbf{\Phi}^{(s,3)} \equiv \mathbf{r}_i + \mathbf{A}_i \mathbf{s}_i'^P - \mathbf{r}_j - \mathbf{A}_j \mathbf{s}_j'^P = \mathbf{0} \tag{6.14}$$

The three scalar constraint equations implied by (6.14) restrict the relative position of points P_i and P_j. Therefore three relative degrees of freedom are maintained between two bodies that are connected by a perfect spherical joint.

An ideal three-dimensional revolute or rotational joint between bodies i and j, shown in Fig. 6.3, is built with a journal–bearing that allows a relative rotation about a common axis, but precludes relative translation along this axis. Equation (6.14) is imposed on an arbitrary point P on the joint axis. Two other points Q_i on body i and Q_j on body j are also arbitrarily chosen on the joint axis. It is clear that vectors $\mathbf{s}_i$ and $\mathbf{s}_j$ must remain parallel. Therefore there are five constraint equations for an ideal three-dimensional revolute joint (Nikravesh 1988):

$$\mathbf{\Phi}^{(r,5)} \equiv \begin{cases} \mathbf{r}_i + \mathbf{A}_i \mathbf{s}_i'^P - \mathbf{r}_j - \mathbf{A}_j \mathbf{s}_j'^P = \mathbf{0} \\ \tilde{\mathbf{s}}_i \mathbf{s}_j = \mathbf{0} \end{cases} \tag{6.15}$$

Note that the cross product in (6.15) has only two independent constraints, the third being linearly dependent on the first two. The five scalar constraint equations

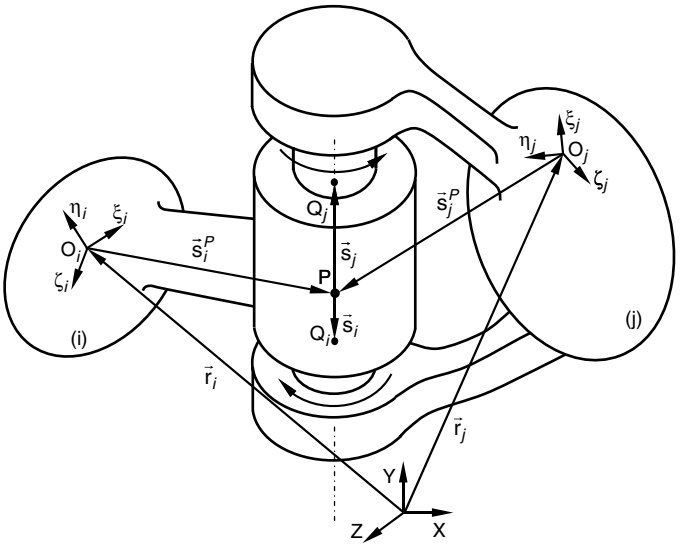

Fig. 6.3 Ideal three-dimensional or spatial revolute joint in a multibody system

yield only one relative degree of freedom for this joint, that is, rotation about the common axis of the revolute joint.

6.2 Spherical Joint with Clearance

In this section, a mathematical model of spherical joint with clearance for spatial multibody systems is presented. In standard multibody models, it is assumed that the connecting points of two bodies, linked by an ideal or perfect spherical joint, are coincident. The introduction of the clearance in a spherical joint separates these two points and the bodies become free to move relative to each other. Hence the three kinematic constraints shown in (6.14) are removed and three relative DOF are allowed instead. A spherical joint with clearance does not constrain any DOF from the system like the ideal spherical joint. In a spherical clearance joint, the dynamics of the joint is controlled by contact-impact forces that result from the collision between the bodies connected. Thus these types of joints can be called as force-joints, since they deal with force constraints instead of kinematic constraints.

Figure 6.4 depicts two bodies i and j connected by a spherical joint with clearance. A spherical part of body j, the ball, is inside of a spherical part of body i, the socket. The radii of socket and ball are R_i and R_j, respectively. The difference in radius between the socket and the ball defines the size of radial clearance, $c = R_i - R_j$. The centers of mass of bodies i and j are O_i and O_j, respectively. Body-fixed coordinate systems $\xi\eta\zeta$ are attached at their center of mass, while XYZ represents the global coordinate system. Point P_i indicates the center of the socket, the center of the ball being denoted by P_j. The vector that connects the point P_i to

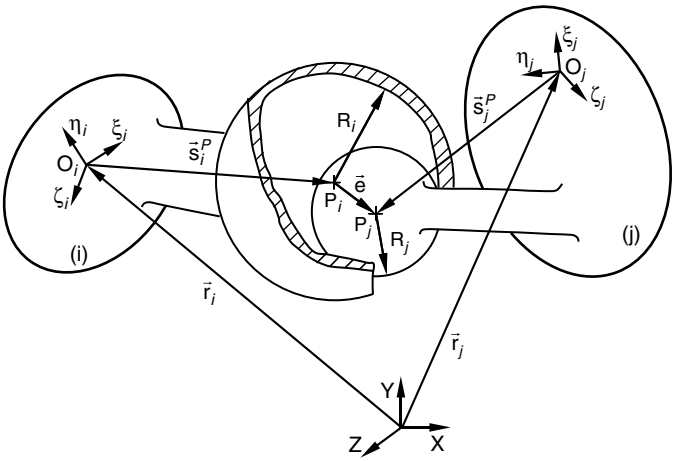

Fig. 6.4 Generic spherical joint with clearance in a multibody system

point P_j is defined as the eccentricity vector, which is represented in Fig. 6.4. Note that, in real mechanisms, the magnitude of the eccentricity is typically much smaller than the radius of the socket and ball.

Similar to the two-dimensional revolute joint, when some amount of clearance is included in a spherical joint, the ball and socket can move relative to each other. Figure 6.5 illustrates the different types of ball motion inside the socket, namely, contact or following mode, free flight mode and impact mode.

In the contact or following mode, the ball and the socket are in permanent contact and a sliding motion relative to each other exists. This mode ends when the ball

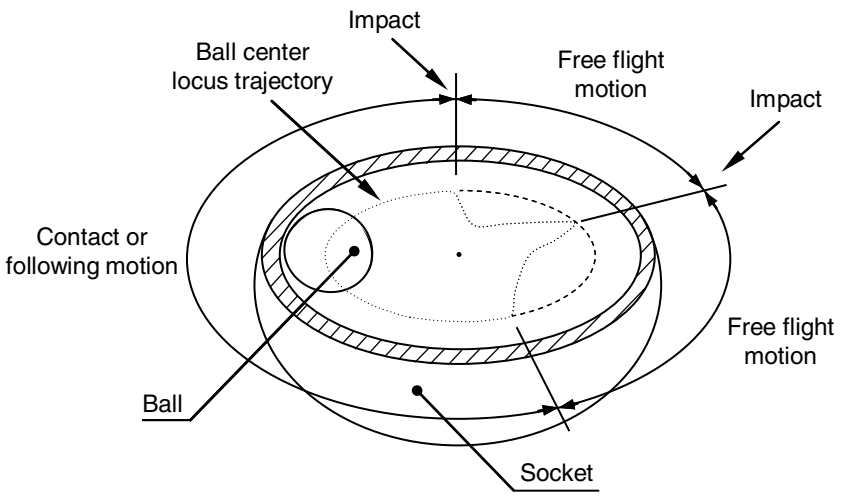

Fig. 6.5 Modes of the ball motion inside the socket

and socket separate from each other and the ball enters the free flight mode. In the free flight motion, the ball moves freely inside the socket boundaries, that is, the ball and the socket are not in contact, hence there is no joint reaction force. In the impact mode, which occurs at the termination of the free flight motion, impact forces are applied to the system. This mode is characterized by an abrupt discontinuity in the kinematic and dynamic responses, and a significant exchange of momentum between the two impacting bodies is observed. At the termination of the impact mode, the ball can enter either the free flight or the following mode.

In what follows, some of the most relevant kinematic aspects related to the spherical clearance joint are presented. As displayed in Fig. 6.4, the eccentricity vector **e**, which connects the centers of the socket and the ball, is given by

$$\mathbf{e} = \mathbf{r}_j^P - \mathbf{r}_i^P \tag{6.16}$$

where both $\mathbf{r}_j^P$ and $\mathbf{r}_i^P$ are described in global coordinates with respect to the inertial reference frame (Nikravesh 1988):

$$\mathbf{r}_k^P = \mathbf{r}_k + \mathbf{A}_k \mathbf{s}_k'^P, \quad (k = i, j) \tag{6.17}$$

The magnitude of the eccentricity vector is evaluated as

$$e = \sqrt{\mathbf{e}^T \mathbf{e}} \tag{6.18}$$

The magnitude of the eccentricity vector expressed in the global coordinates is written as

$$e = \sqrt{(x_j^P - x_i^P)^2 + (y_j^P - y_i^P)^2 + (z_j^P - z_i^P)^2} \tag{6.19}$$

and the time rate of change of the eccentricity in the radial direction, that is, in the direction of the line of centers of the socket and the ball is

$$\dot{e} = \frac{(x_j^P - x_i^P)(\dot{x}_j^P - \dot{x}_i^P) + (y_j^P - y_i^P)(\dot{y}_j^P - \dot{y}_i^P) + (z_j^P - z_i^P)(\dot{z}_j^P - \dot{z}_i^P)}{e} \tag{6.20}$$

in which the dot denotes the derivative with respect to time.

A unit vector **n** normal to the collision surface between the socket and the ball is aligned with the eccentricity vector, as observed in Fig. 6.6. Thus

$$\mathbf{n} = \frac{\mathbf{e}}{e} \tag{6.21}$$

Figure 6.6 illustrates the situation in which the socket and the ball bodies are in contact, which is identified by the existence of a relative penetration. The contact or control points on bodies i and j are Q_i and Q_j, respectively. The global position of the contact points in the socket and ball are given by

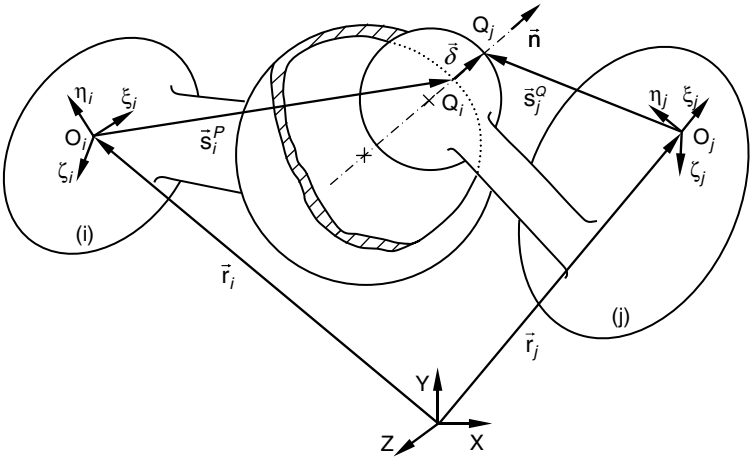

Fig. 6.6 Penetration depth between the socket and the ball during the contact

$$\mathbf{r}_k^Q = \mathbf{r}_k + \mathbf{A}_k \mathbf{s}_k'^Q + R_k \mathbf{n}, \quad (k = i, j) \tag{6.22}$$

where R_i and R_j are radius of the socket and the ball, respectively.

The velocity of the contact points Q_i and Q_j in the global system is obtained by differentiating (6.22) with respect to time, yielding

$$\dot{\mathbf{r}}_k^Q = \dot{\mathbf{r}}_k + \dot{\mathbf{A}}_k \mathbf{s}_k'^Q + R_k \dot{\mathbf{n}}, (k = i, j) \tag{6.23}$$

Let the components of the relative velocity of contact points in the normal and tangential direction to the surface of collision be represented by $\mathbf{v}_N$ and $\mathbf{v}_T$, respectively. The relative normal velocity determines whether the contact bodies are approaching or separating, and the relative tangential velocity determines whether the contact bodies are sliding or sticking. The relative scalar velocities, normal and tangential to the surface of collision, are obtained by projecting the relative impact velocity onto the tangential and normal directions, yielding

$$\mathbf{v}_N = [(\dot{\mathbf{r}}_j^Q - \dot{\mathbf{r}}_i^Q)^T \mathbf{n}]\mathbf{n} \tag{6.24}$$

$$\mathbf{v}_T = (\dot{\mathbf{r}}_j^Q - \dot{\mathbf{r}}_i^Q)^T - \mathbf{v}_N \equiv v_T \mathbf{t} \tag{6.25}$$

where $\mathbf{t}$ represents the tangential direction to the impacted surfaces.

From Fig. 6.6 it is clear that the geometric condition for contact between the socket and the ball can be defined as

$$\delta = e - c \tag{6.26}$$

where e is the magnitude of the eccentricity vector given by (6.18) and c is the radial clearance size. It should be noted here that the clearance is taken as a specified parameter. When the magnitude of the eccentricity vector is smaller than the radial

clearance size there is no contact between the socket and the ball and, consequently, they can freely move relative to each other. When the magnitude of eccentricity is larger than radial clearance, there is contact between the socket and the ball, the relative penetration being given by (6.26). Then a constitutive contact law, such as the continuous contact force model proposed by Lankarani and Nikravesh (1990), expressed by (3.9), is applied in order to evaluate the contact force developed in the direction perpendicular to the plane of collision. Thus the magnitude of the contact force can be summarized as follows:

$$F_N = \begin{cases} 0 & \text{if } \delta < 0 \\ K\delta^n \left[1 + \dfrac{3(1-c_e^2)}{4} \dfrac{\dot{\delta}}{\dot{\delta}^{(-)}} \right] & \text{if } \delta > 0 \end{cases} \tag{6.27}$$

where the generalized parameter K is evaluated by (3.3), c_e is the restitution coefficient, $\dot{\delta}$ is the relative penetration velocity and $\dot{\delta}^{(-)}$ is the initial impact velocity. The nature of the contact forces for spatial systems is identical to those for planar systems, which are presented and discussed in Chap. 3.

The normal and tangential forces at the contact points are represented by $\mathbf{f}_N$ and $\mathbf{f}_T$, respectively. Since these forces do not act through the center of mass of bodies i and j, the moment components for each body need to be evaluated. Furthermore the contribution of the contact forces to the generalized force vector is obtained by projecting the normal and tangential forces onto the X, Y and Z directions. Based on Fig. 6.7, the equivalent forces and moments applied on the center of mass of body i are given by

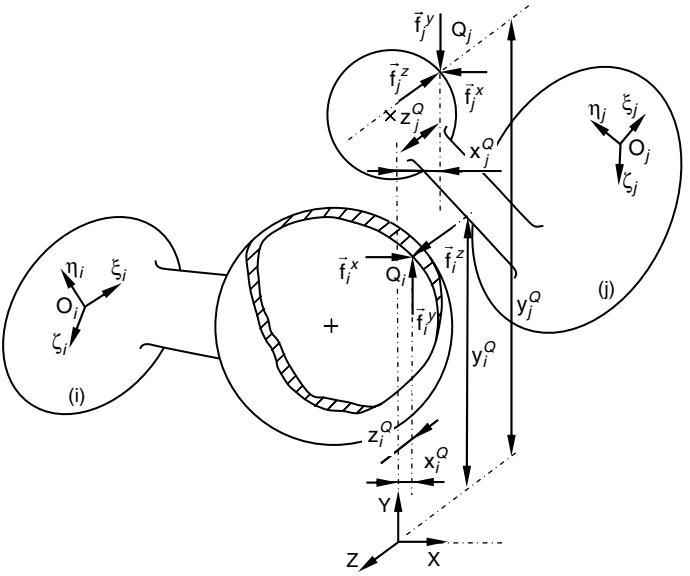

Fig. 6.7 Penetration depth between the socket and the ball during the contact

$$\mathbf{f}_i = \mathbf{f}_N + \mathbf{f}_T \tag{6.28}$$

$$\mathbf{m}_i = \tilde{\mathbf{s}}_i^Q \mathbf{f}_i \tag{6.29}$$

The forces and moments acting on body j are written as

$$\mathbf{f}_j = -\mathbf{f}_i \tag{6.30}$$

$$\mathbf{m}_j = -\tilde{\mathbf{s}}_j^Q \mathbf{f}_i \tag{6.31}$$

For notation purpose the tilde ($\sim$) placed over a vector indicates that the components of the vector are used to generate a skew-symmetric matrix (Nikravesh 1988).

6.3 Spatial Revolute Joint with Clearance

The typical configuration of a spatial revolute joint with clearance is schematically illustrated in Fig. 6.8. The pair of elements in a spatial revolute clearance joint are a cylindrical hole, the bearing, and a cylindrical pin, the journal. The clearance, in a realistic connection, is much smaller than the length of the two cylinders or the nominal radius of the joint elements.

Similar to the spherical clearance joint model development, the two mechanical bodies connected by the joint are modeled as colliding bodies, and, consequently, contact-impact forces control the dynamics of the joint. In the methodology presented here, the contact force model with hysteric damping is used to evaluate the normal contact forces resulting from the interpenetration between the journal and the bearing. For this purpose, the mechanical elements are considered as two rigid bodies in contact that penetrate into each other, without deforming. The normal contact force depends on this pseudo-penetration, according to the model proposed by Lankarani and Nikravesh (1990). Thus it is clear that the spatial revolute joint with clearance does not impose any kinematic constraint to the system, but imposes some force restrictions, limiting the journal movement within the bearing limits.

The model for the spatial revolute clearance joint is more complex than the spherical joint with clearance, because there are more paths of motion for the journal when clearance is present. Four different types of journal motion inside the bearing are considered in the present work, namely: (1) free flight motion where there is

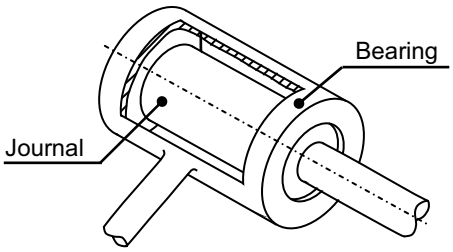

Fig. 6.8 Typical spatial revolute joint with clearance

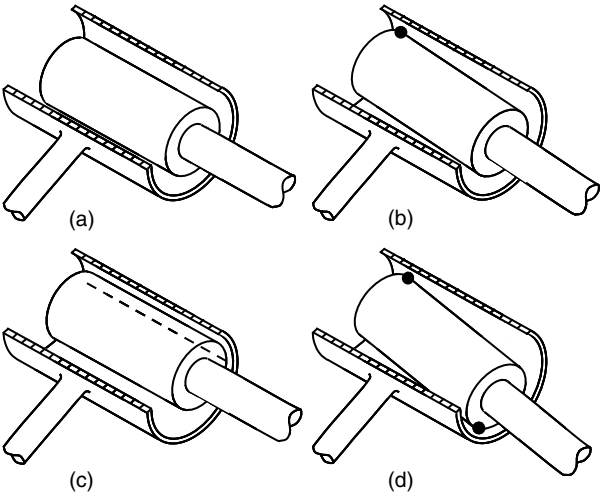

Fig. 6.9 Four different possible scenarios for the journal motion relative to the bearing: (**a**) no contact; (**b**) one point contact; (**c**) line contact; (**d**) two contact points in opposite sides

no contact between the two elements; (2) the journal contacts with the bearing wall at a point; (3) the journal and bearing contact with each other at a line; (4) two contact points between the journal and the bearing wall, but in opposite sides. These four possibilities are illustrated in Fig. 6.9. The dynamic response of the joint is a function of these four scenarios which depend on the system configuration.

In a noncontact situation, no forces are introduced into the system, because the journal moves freely inside the bearing boundaries until it reaches the bearing wall. When the journal and the bearing are in contact with each other, local deformations take place at the contact area and, consequently, contact-impact forces characterize the interaction between the bodies. By evaluating the variation of the contact forces during the contact period, the system response is obtained simply by adding the contact-impact forces to the multibody system equations of motion as external generalized forces. This approach provides accurate results, in so far as the equations of motion are integrated over the period of contact. It, thus, accounts for the changes in the configuration and velocities of the system during that contact.

In order for the spatial revolute clearance joints to be used in the multibody system formulation, it is required that a mathematical model be developed. Figure 6.10 shows a representation of a spatial revolute joint with clearance that connects bodies i and j. The bearing is part of body i and the journal is part of body j. The difference in radius between the bearing and the journal, $c = R_i - R_j$, defines the size of the radial clearance. The center of mass of bodies i and j are O_i and O_j, respectively. Body-fixed coordinate systems $\xi\eta\zeta$ are attached at the center of mass of each body, whereas the XYZ denotes the global coordinate system. The geometric center of the bearing is located at point P which, together with point Q, defines the joint/bearing axis, while points V and W on body j define the journal axis. These points are

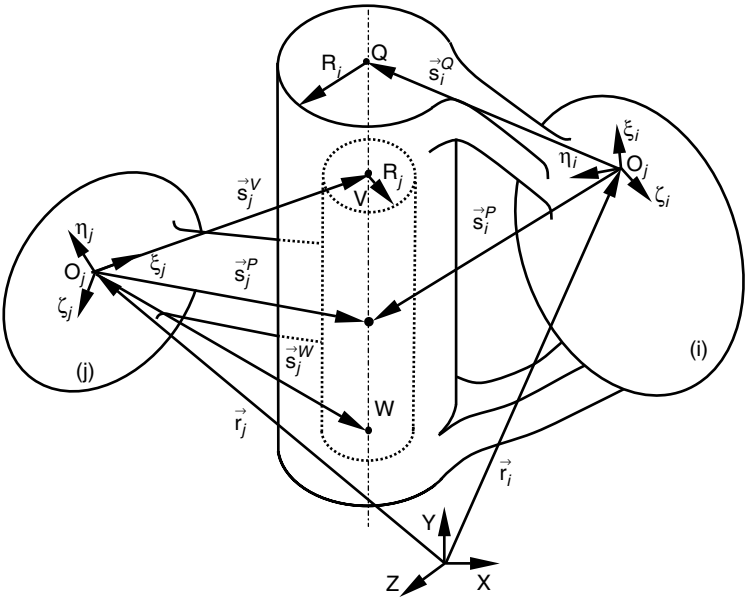

Fig. 6.10 General configuration of a three-dimensional or spatial revolute joint with clearance in a multibody system

located at the top and bottom of journal bases, so that the distance between points V and W defines the length of the joint.

Figure 6.11 shows two different scenarios for the contact between the journal and the bearing. For simplicity, in this figure only the journal and the bearing are

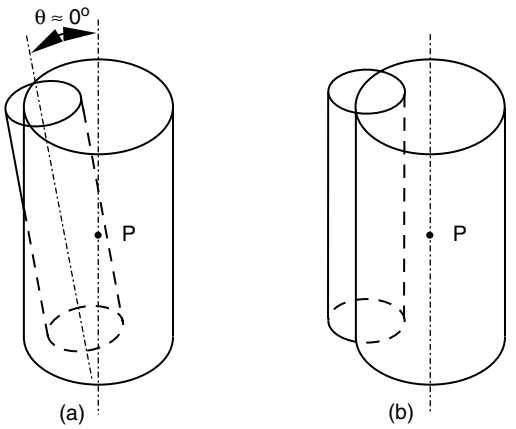

Fig. 6.11 Two different scenarios for contact between the journal and the bearing wall: (**a**) only one journal base (top) contacts with the bearing wall; (**b**) both bases (top and bottom) contact with the bearing wall

represented. In the present methodology, only the top and the bottom journal bases are considered for contact detection between the journal and bearing elements. Furthermore it is assumed that the clearance is much smaller than the dimensions of the bodies, so that the angle between the bearing and journal axes, represented by θ in Fig. 6.11a, is very small and, consequently, both top and bottom journal bases can be assumed to be parallel and perpendicular to the joint axis, as illustrated in Fig. 6.12.

Assuming a local coordinate system $(\xi\eta\zeta)_r$ associated with the revolute clearance joint axis located at point P, the unit coordinate vectors defined along the local axes are $\mathbf{u}'_\xi$, $\mathbf{u}'_\eta$ and $\mathbf{u}'_\xi$, as illustrated in Fig. 6.13. The unit coordinate vector along the ζ_r-axis, $\mathbf{u}'_\xi$, is evaluated as

$$\mathbf{u}'_\xi = \frac{\mathbf{s}_i'^Q - \mathbf{s}_i'^P}{\left\| \mathbf{s}_i'^Q - \mathbf{s}_i'^P \right\|} \tag{6.32}$$

where both vectors $\mathbf{s}_i'^P$ and $\mathbf{s}_i'^Q$ are described in the local coordinate system of body i. The remaining two unit vectors are evaluated according to

$$\begin{cases} \mathbf{u}'_\xi = \mathbf{u}'_\xi \\ \mathbf{u}'_\eta = \mathbf{u}'_\eta \end{cases} \quad \text{if} \quad \mathbf{u}'_\xi = \mathbf{u}'_\zeta \tag{6.33}$$

or

$$\begin{cases} \mathbf{u}'_\xi = \tilde{\mathbf{u}}'_{\zeta_r}\, \mathbf{u}'_{\zeta_i} \\ \mathbf{u}'_\eta = \tilde{\mathbf{u}}'_{\zeta_r}\, \mathbf{u}'_{\xi_r} \end{cases} \quad \text{if} \quad \mathbf{u}'_\xi \neq \mathbf{u}'_\zeta \tag{6.34}$$

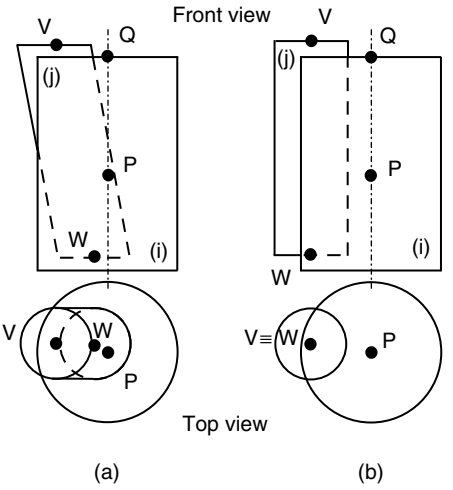

Fig. 6.12 Front and top views for contact between the journal and the bearing: (**a**) only the journal top base contacts with the bearing wall; (**b**) both journal bases (top and bottom) contact with the bearing wall

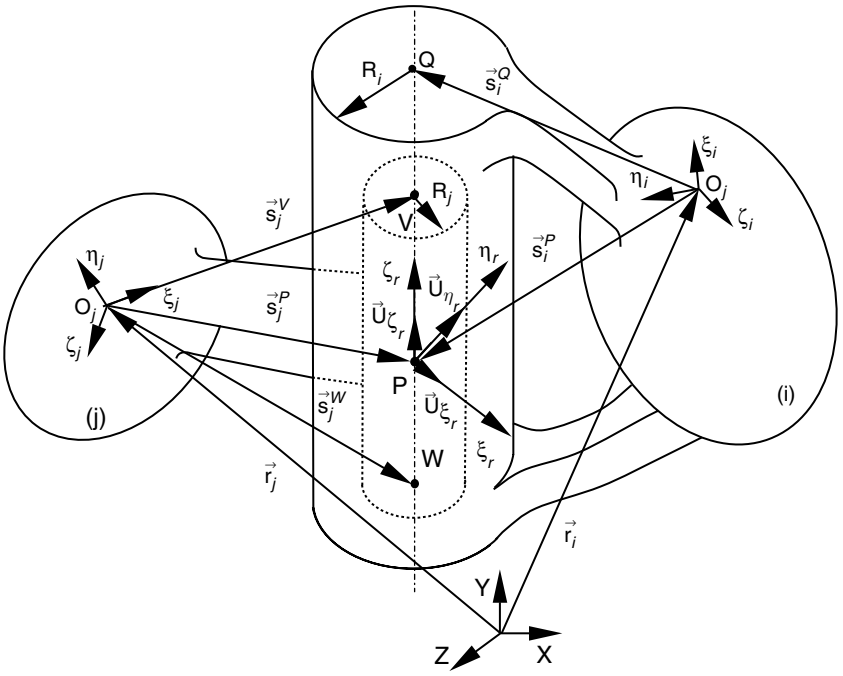

Fig. 6.13 Definition of the local coordinate system associated with the revolute clearance joint and the respective unit vectors

The transformation matrix $\mathbf{A}_{ri}$ from local components $(\xi\eta\zeta)_r$ into the local coordinate system $(\xi\eta\zeta)_i$ is expressed as (Nikravesh 1988)

$$\mathbf{A}_{ri} = [\,\mathbf{u}'_\xi \;\mathbf{u}'_\eta \;\mathbf{u}'_\xi\,]^{\mathrm{T}} \tag{6.35}$$

Note that this transformation matrix is constant. Furthermore if $\mathbf{u}'_\xi = \mathbf{u}'_\xi$ the transformation matrix $\mathbf{A}_{ri}$ is the identity matrix $\mathbf{I}$. Thus the matrix that transforms the local vectors $(\xi\eta\zeta)_r$ into the global reference system XYZ is given by

$$\mathbf{A}_r = \mathbf{A}_i \mathbf{A}_{ri} \tag{6.36}$$

The global position of the origin of the local coordinate system $(\xi\eta\zeta)_r$ is

$$\mathbf{r}_i^P = \mathbf{r}_i + \mathbf{A}_i \mathbf{s}'_{iP} \tag{6.37}$$

In order to define the relative position between the journal and the bearing, it is necessary to express the vectors $\mathbf{s}_j^V$ and $\mathbf{s}_j^W$ in the local coordinate system associated with the joint $(\xi\eta\zeta)_r$. From Fig. 6.13, the global coordinates of points V and W with respect to the inertial reference frame are expressed as

$$\mathbf{r}_j^V = \mathbf{r}_j + \mathbf{A}_j \mathbf{s}'^V_j \tag{6.38}$$

$$\mathbf{r}_j^W = \mathbf{r}_j + \mathbf{A}_j \mathbf{s}'^W_j \tag{6.39}$$

Thus vectors $\mathbf{s}_j^V$ and $\mathbf{s}_j^W$ expressed in the global coordinate system are

$$\mathbf{s}_r^V = \mathbf{r}_j^V - \mathbf{r}_i^P \tag{6.40}$$

$$\mathbf{s}_r^W = \mathbf{r}_j^W - \mathbf{r}_i^P \tag{6.41}$$

When expressed in the local coordinate system of the joint, these vectors are given by

$$\mathbf{s}'^V_r = \mathbf{A}_r^T \mathbf{s}_r^V \tag{6.42}$$

$$\mathbf{s}'^W_r = \mathbf{A}_r^T \mathbf{s}_r^W \tag{6.43}$$

The vectors given by (6.42) and (6.43) define the coordinates of points V and W of the journal, expressed in terms of the local coordinate system associated with the joint, that is, $(\xi\eta\zeta)_r$.

Figure 6.14 depicts a configuration for the system in which both top and bottom journal bases contact with the bearing wall. The eccentricity vectors at the top and bottom journal bases, $\mathbf{e}_r^V$ and $\mathbf{e}_r^W$, are given by the projection of the vectors $\mathbf{s}_r^V$ and $\mathbf{s}_r^W$ onto the local axes ξ_r and η_r, yielding

$$\mathbf{e}_r^V = \{(\mathrm{s}'^V_r)_{\xi_r} \quad (\mathrm{s}'^V_r)_{\eta_r} \quad 0\}^T \tag{6.44}$$

$$\mathbf{e}_r^W = \{(\mathrm{s}'^W_r)_{\xi_r} \quad (\mathrm{s}'^W_r)_{\eta_r} \quad 0\}^T \tag{6.45}$$

The magnitudes of the eccentricity vectors are evaluated as

$$\mathrm{e}_r^V = \sqrt{(\mathbf{e}_r^V)^T \, \mathbf{e}_r^V} \tag{6.46}$$

$$\mathrm{e}_r^W = \sqrt{(\mathbf{e}_r^W)^T \, \mathbf{e}_r^W} \tag{6.47}$$

The unit vectors, $\mathbf{n}_r^V$ and $\mathbf{n}_r^W$, are normal to the planes of contact at the points where the top and bottom journal bases touch the bearing wall. Referring to Fig. 6.14 these normal vectors are evaluated as

$$\mathbf{n}_r^V = \frac{\mathbf{e}_r^V}{\left\| \mathbf{e}_r^V \right\|} \tag{6.48}$$

$$\mathbf{n}_r^W = \frac{\mathbf{e}_r^W}{\left\| \mathbf{e}_r^W \right\|} \tag{6.49}$$

Referring to Fig. 6.14, the penetrations due to the contact between the journal bases and the bearing wall are calculated as

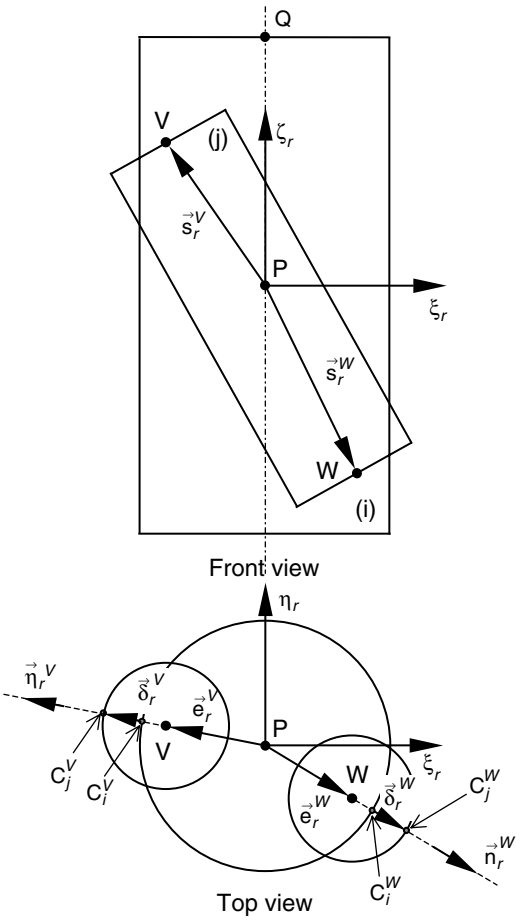

Fig. 6.14 Definition of the local coordinate system associated with the revolute clearance joint and the respective unit vectors

$$\delta_r^V = e_r^V - c \tag{6.50}$$

$$\delta_r^W = e_r^W - c \tag{6.51}$$

where e_r^V and e_r^W are, respectively, the modules of the eccentricity vectors at the top and bottom journal bases, and c is the radial clearance given by the difference between the radius of the bearing and the journal. There is contact if the radial motion exceeds the radial clearance size.

Considering C_i^V, C_j^V, C_i^W and C_j^W to be the potential contact points on bodies i and j, their global positions are evaluated as

$$\mathbf{r}_k^{C_k^V} = \mathbf{r}_k^P + \mathbf{A}_k \mathbf{s}'^{C_k^V}_k, \quad (k = i, j) \tag{6.52}$$

$$\mathbf{r}_k^{C_k^W} = \mathbf{r}_k^P + \mathbf{A}_k \mathbf{s}'^{C_k^W}_k, \quad (k = i, j) \tag{6.53}$$

where vectors $\mathbf{s}'^{C_k^V}_k$ and $\mathbf{s}'^{C_k^W}_k$, $(k = i, j)$, are the local coordinates of vectors $\mathbf{s}^{C_k^V}_k$ and $\mathbf{s}^{C_k^W}_k$ on bodies i and j, expressed by the local coordinate system of each body. These vectors are only defined in the local coordinate system of the joint $(\xi\eta\zeta)_r$ and are expressed as

$$\mathbf{s}'^{C_i^V}_r = \{0\ 0\ (\mathbf{s}'^{V}_r)_{\zeta_r}\}^T + R_i\mathbf{n}^V_r \tag{6.54}$$

$$\mathbf{s}'^{C_j^V}_r = \mathbf{s}'^{V}_r + R_j\mathbf{n}^V_r \tag{6.55}$$

$$\mathbf{s}'^{C_i^W}_r = \{0\ 0\ (\mathbf{s}'^{W}_r)_{\zeta_r}\}^T + R_i\mathbf{n}^W_r \tag{6.56}$$

$$\mathbf{s}'^{C_j^W}_r = \mathbf{s}'^{W}_r + R_j\mathbf{n}^W_r \tag{6.57}$$

The vectors defined by (6.54)–(6.57) when expressed in the local coordinate systems associated with bodies i and j yield

$$\mathbf{s}'^{C_i^V}_i = \mathbf{A}_{ri}\mathbf{s}'^{C_i^V}_r \tag{6.58}$$

$$\mathbf{s}'^{C_j^V}_j = \mathbf{A}^T_j\mathbf{A}_r\mathbf{s}'^{C_j^V}_r \tag{6.59}$$

$$\mathbf{s}'^{C_i^W}_i = \mathbf{A}_{ri}\mathbf{s}'^{C_i^W}_r \tag{6.60}$$

$$\mathbf{s}'^{C_j^W}_j = \mathbf{A}^T_j\mathbf{A}_r\mathbf{s}'^{C_j^W}_r \tag{6.61}$$

The impact velocities, required to evaluate the contact forces, using the Lankarani and Nikravesh model, are obtained by differentiating (6.52) and (6.53) with respect to time, yielding

$$\dot{\mathbf{r}}^{C_k^V}_k = \dot{\mathbf{r}}^P_k + \mathbf{A}_k\tilde{\boldsymbol{\omega}}'_k\mathbf{s}'^{C_k^V}_k, \quad (k = i, j) \tag{6.62}$$

$$\dot{\mathbf{r}}^{C_k^W}_k = \dot{\mathbf{r}}^P_k + \mathbf{A}_k\tilde{\boldsymbol{\omega}}'_k\mathbf{s}'^{C_k^W}_k, \quad (k = i, j) \tag{6.63}$$

The relative impact velocities between the two bodies at the contact points are

$$\Delta\dot{\mathbf{r}}^V = \dot{\mathbf{r}}^{C_j^V}_j - \dot{\mathbf{r}}^{C_i^V}_i \tag{6.64}$$

$$\Delta\dot{\mathbf{r}}^W = \dot{\mathbf{r}}^{C_j^W}_j - \dot{\mathbf{r}}^{C_i^W}_i \tag{6.65}$$

The relative velocities given by (6.64) and (6.65) are projected onto the direction normal to the penetration, yielding the relative normal velocities, $\dot{\delta}^V_r$ and $\dot{\delta}^W_r$, shown in Fig. 6.15. The normal relative velocities represent whether the contact bodies are approaching or separating. These velocities are evaluated by

$$\dot{\delta}^V_r = (\Delta\dot{\mathbf{r}}^V)^T\mathbf{n}^V_r \tag{6.66}$$

$$\dot{\delta}^W_r = (\Delta\dot{\mathbf{r}}^W)^T\mathbf{n}^W_r \tag{6.67}$$

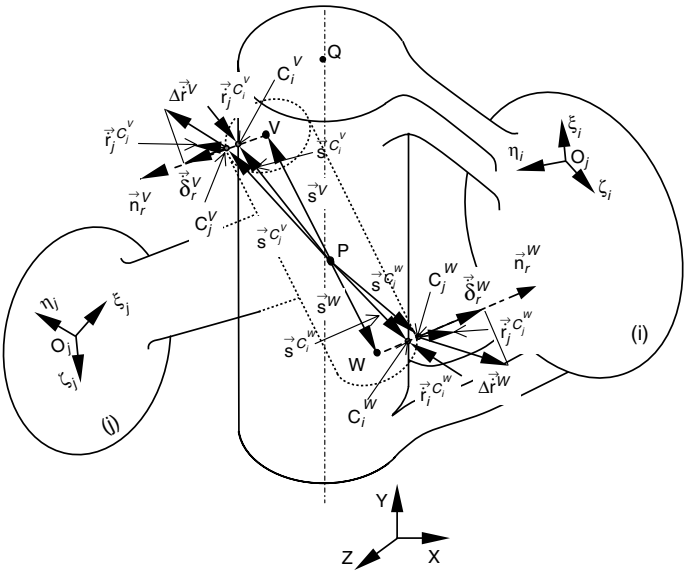

Fig. 6.15 Location of the contact points and representation of impact velocities

When contact between the journal and the bearing takes place, impact forces act at the contact points. The contributions of these impact forces to the generalized vector of forces are found by projecting them onto the X, Y and Z directions. Since these forces do not act through the center of mass of the bodies i and j, the moment components for each body need to be evaluated. For convenience and simplicity the bodies are presented separately in Fig. 6.16 and only the force components that act at the top journal base are illustrated. According to Fig. 6.16, the forces and moments working on the center of mass of body i are given by

$$\mathbf{f}_i = \mathbf{f}_N + \mathbf{f}_T \tag{6.68}$$

$$\mathbf{m}_i = y_i^{C_i^V}\mathbf{f}_i^z - z_i^{C_i^V}\mathbf{f}_i^y + x_i^{C_i^V}\mathbf{f}_i^z - z_i^{C_i^V}\mathbf{f}_i^x + x_i^{C_i^V}\mathbf{f}_i^y - y_i^{C_i^V}\mathbf{f}_i^x \tag{6.69}$$

The forces and moments corresponding to body j are written as

$$\mathbf{f}_j = -\mathbf{f}_i \tag{6.70}$$

$$\mathbf{m}_j = -y_j^{C_j^V}\mathbf{f}_j^z + z_j^{C_j^V}\mathbf{f}_j^y - x_j^{C_j^V}\mathbf{f}_j^z + z_j^{C_j^V}\mathbf{f}_j^x - x_j^{C_j^V}\mathbf{f}_j^y + y_j^{C_j^V}\mathbf{f}_j^x \tag{6.71}$$

Since the formulation of the spatial revolute joint involves a good deal of mathematical manipulation, it is convenient to summarize the main steps in an appropriate algorithm. This algorithm, presented in the flowchart of Fig. 6.17, is developed in the framework of the multibody methodology and can be condensed in the following steps:

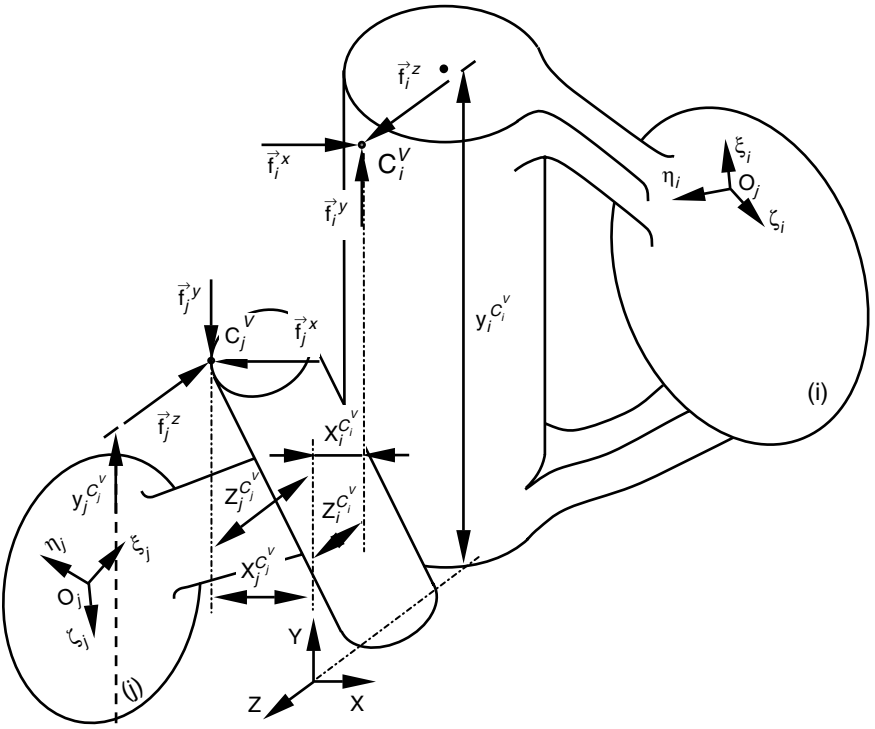

Fig. 6.16 Contact forces defined at the points of contact

1. Start at instant of time t^0, with given initial conditions for positions $\mathbf{q}^0$ and velocities $\dot{\mathbf{q}}^0$.
2. Define the location of points P_i, P_j, Q_i, V_j and W_j, necessary to describe the spatial revolute clearance joint. Define joint and material properties (R_B, E_B, ν_B, R_J, E_J and ν_J).
3. Compute the local coordinate system associated with the joint, $(\xi\eta\zeta)r$ and evaluate the unit coordinate vectors along each axis, that is, $\mathbf{u}'_\xi$, $\mathbf{u}'_\eta$ and $\mathbf{u}'_\xi$ using (6.32)–(6.34).
4. Evaluate the local coordinates of the geometrical centers of the top and bottom bases in the $(\xi\eta\zeta)r$ system using (6.42)–(6.43).
5. Compute eccentricity vectors $\mathbf{e}_r^V$ and $\mathbf{e}_r^W$ and the unit vectors that define the impact direction $\mathbf{n}_r^V$ and $\mathbf{n}_r^W$ through (6.44)–(6.49).
6. Evaluate the penetrations δ_r^V and δ_r^W with (6.50)–(6.51).
7. Check for contact: if there is contact, determine the contact points using (6.52)–(6.53), evaluate the impact velocities with (6.66)–(6.67), compute the impact forces by (6.68)–(6.71) and add the impact forces to the equations of motion.
8. Obtain the new positions and velocities of the system for time step $t + \Delta t$ by integration of the final derivatives of the state variables.

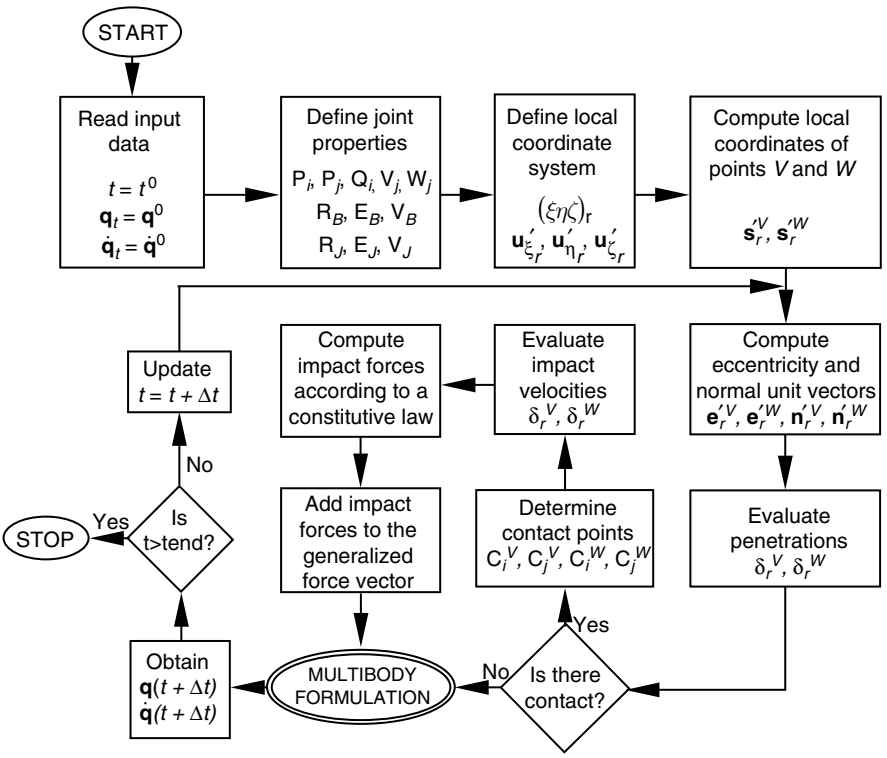

Fig. 6.17 Representation of the algorithm proposed to model spatial revolute joint with clearance in multibody systems

9. Update the system time variable.
10. Go to step 5 and repeat the whole process for the new time step, until the final time for the analysis is reached.

6.4 Demonstrative Example 1: Four-Bar Mechanism

In this section, the application of the four-bar mechanism that describes a spatial motion (Haug 1989) is employed, as an illustrative example to demonstrate how a spherical clearance joint can affect the behavior of the mechanism. The spatial four-bar mechanism consists of four rigid bodies that represent the ground, crank, coupler and rocker. The body numbers and their corresponding local coordinate systems are shown in Fig. 6.18. The kinematic joints of this multibody system include two ideal revolute joints, connecting the ground to the crank and the ground to the rocker, and one perfect spherical joint that connects the crank and coupler. A spherical joint, with a given clearance, interconnects the coupler and the rocker. This four-bar mechanism is modeled with 24 coordinates, which result from 4 rigid bodies and 19 kinematic constraints. Consequently this system has five degrees of freedom.

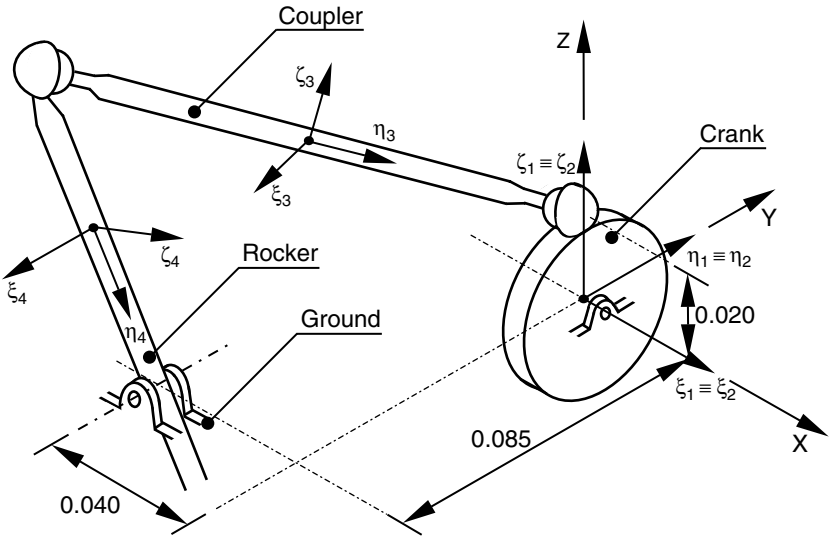

Fig. 6.18 Representation of the algorithm proposed to model spatial revolute joint with clearance in multibody systems

The initial configuration of the spatial four-bar mechanism is illustrated in Fig. 6.18. The system is released from the initial position with null velocities and under the action of gravity force, which is taken to act in the negative Z direction. The dimensions and inertia properties of each body are presented in Table 6.1. The dynamic parameters used for the simulation and for the numerical methods required to solve the system dynamics are listed in Table 6.2.

In order to study the influence of the spherical clearance model in the global behavior of the spatial four-bar mechanism, some kinematic and dynamic characteristics, corresponding to the first 2s of the simulation, are presented and discussed in what follows. The results are always plotted against those obtained with a simulation in which all kinematic joints are considered to be ideal or perfect.

The normal contact force and the joint reaction force, for the first impact at the spherical clearance joint, are shown in Fig. 6.19a. The plotted reaction force is the magnitude of the joint force in the revolute joint that connects the ground to the rocker. The simulation is performed by employing the Lankarani and Nikravesh contact force model given by (3.9). By observing Fig. 6.19a, it is clear how the impacts inherent to the dynamics of the clearance joint influence the reaction force.

Table 6.1 Geometric and inertia properties of the spatial four-bar mechanism

Body nr	Length (m)	Mass (kg)	Moment of inertia (kg m^2)		
			$I_{\xi\xi}$	$I_{\eta\eta}$	$I_{\zeta\zeta}$
2	0.020	0.0196	0.0000392	0.0000197	0.0000197
3	0.122	0.1416	0.0017743	0.0000351	0.0017743
4	0.074	0.0316	0.0001456	0.0000029	0.0001456

Table 6.2 Parameters used in the dynamic simulation of the four-bar mechanism

Socket radius	10.0 mm	Young's modulus	207 GPa
Ball radius	9.5 mm	Poisson's ratio	0.3
Radial clearance	0.5 mm	Integration step size	0.00001 s
Restitution coefficient	0.9	Integration tolerance	0.000001 s

The two force curves plotted show a very similar shape. The maximum reaction force is about 60% of the contact force. Figure 6.19b shows the hysteresis curves for the first three impacts at the spherical clearance joint. The contact force decreases for each impact suggesting that some system energy is dissipated from impact to impact. This dissipated energy is measured as the area enclosed by the hysteresis plot. The energy dissipation is due to the contact model used and, since the gravitational force is the only external action, that is, no other external forces or drivers are applied to the system, no energy is fed to the system.

Figure 6.20a–d depicts the Z-component for the position, velocity and acceleration of the center of mass of rocker, as well as the Y-component of the reaction moment that acts at the revolute joint that connects the ground to the rocker, for both ideal and spherical clearance joint simulations. The results plotted in Fig. 6.20a show that the position accuracy of the four-bar mechanism is clearly influenced by the effective joint clearance. Furthermore the maximum Z-position is not reached in every cycle since the impacts within the joint with clearance dissipate some of the system's energy. Figure 6.20c and d shows that the mechanism with clearance joint creates significantly larger dynamic accelerations and reaction moments on the system than those observed for an ideal dynamic model. The magnitude of acceleration and moment for the case of the ideal joint is very low, not even visible in the figures, since there is no driver in the system, the gravitational force being the only external action on the system.

The magnitude of the eccentricity vector is plotted in Fig. 6.21, in which the different types of motion between the ball center and the socket center can be observed,

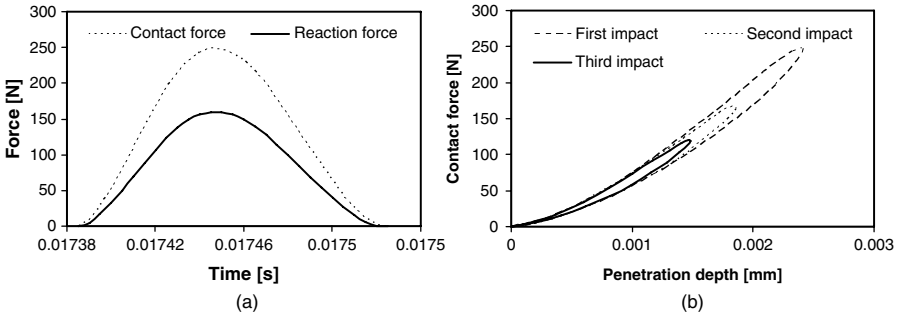

Fig. 6.19 (**a**) Normal contact force at the clearance joint and corresponding reaction force in the ground–rocker revolute joint for the first impact; (**b**) hysteresis loop of the first three impacts at the clearance joint. The contact force decreases from impact to impact because no energy is fed to the system

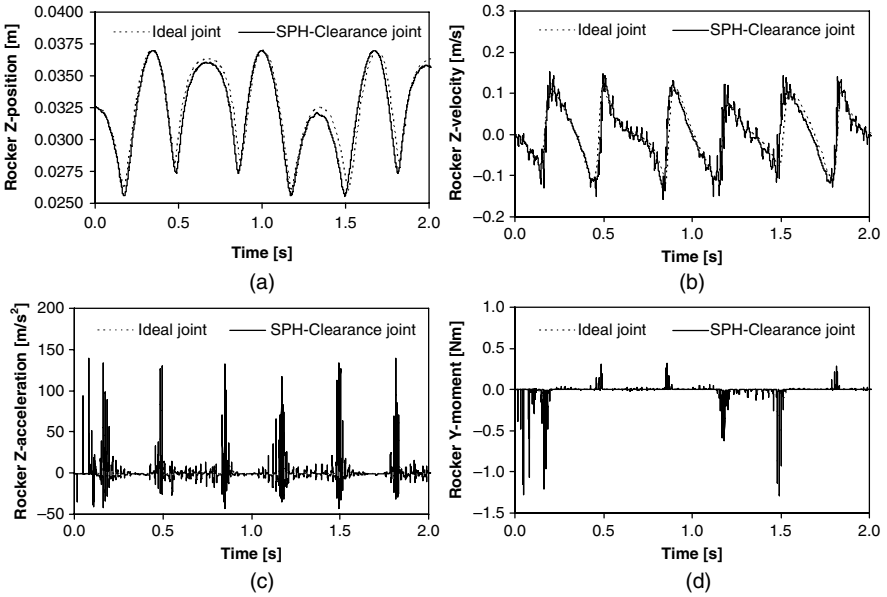

Fig. 6.20 (**a**) Z-coordinate of rocker center of mass; (**b**) Z-velocity of rocker center of mass; (**c**) Z-acceleration of rocker center of mass; (**d**) Y-component of the reaction moment at the ground–rocker revolute joint.

namely, free flight, impact, rebound and permanent or continuous contact. In the first instants of the simulation, free flight motion followed by impacts and rebounds are well evident. After that, it can be observed that the ball and socket present periods of permanent or continuous contact, where the ball follows the socket wall. The dashed line in Fig. 6.21 represents the radial clearance size (0.5 mm), which corresponds to the maximum relative motion between the ball and the socket without contact.

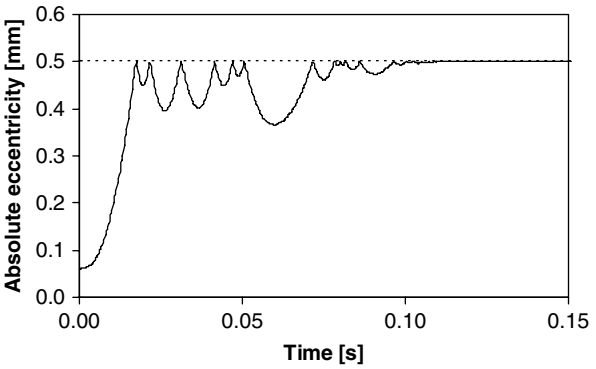

Fig. 6.21 Module of the eccentricity vector

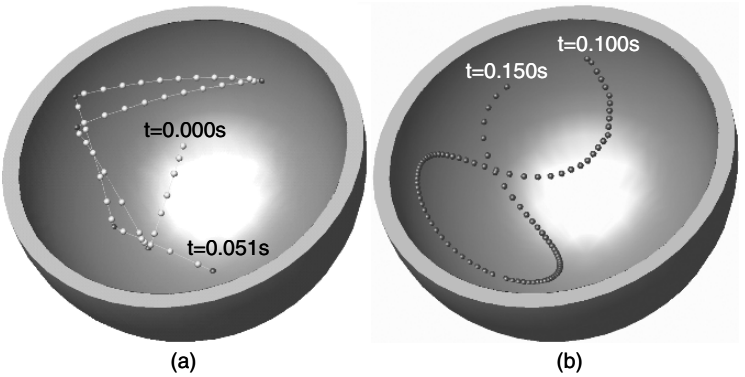

Fig. 6.22 Ball center trajectory inside the socket: (**a**) first simulation's instants in which free flight motion and impacts followed by rebounds are visible; (**b**) permanent or continuous contact, i.e., the ball follows the socket wall

The path of the ball center relative to the socket center is also illustrated in Fig. 6.22. Figure 6.22a shows the relative motion between the two bodies for the first six impacts. The half gray spherical surface represents the clearance limit while the small spheres inside represent the ball center path. The free flights are illustrated by clear spheres, whereas the impacts are represented by darker spheres. It is clear that in the first instants of simulation the impacts are immediately followed by rebounds. Figure 6.22b shows the time interval simulation from 0.100 to 0.150 s. From this figure, it is observed that the ball is always in permanent contact with the socket wall. Furthermore the permanent contact between the ball and socket is accomplished by varying the penetration depth along the radial direction. The Poincaré maps are used to illustrate the dynamic behavior of the spatial four-bar mechanism with a spherical clearance joint. The system's response is nonlinear, as the relative motion between the ball and the socket can change from free flights, impact and continuous contact, as illustrated in Figs. 6.21 and 6.22. The nonlinear system response is well visible by plotting the corresponding Poincaré maps, which relate the rocker Z-velocity versus rocker Z-position, shown in Fig. 6.23. The Poincaré map presented in Fig. 6.23b has a complex aspect, densely filled by orbits or points, which indicates chaotic behavior.

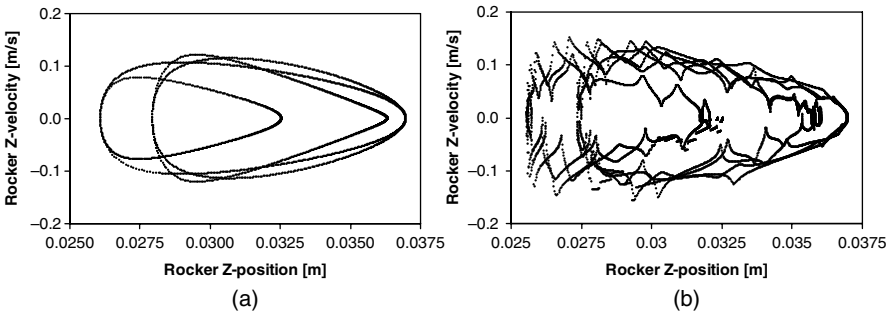

Fig. 6.23 Poincaré maps: (**a**) ideal joint; (**b**) spherical clearance joint

6.5 Demonstrative Example 2: Double Pendulum

In order to examine the effectiveness of the formulation developed for the spatial revolute clearance joint, a double pendulum with the configuration shown in Fig. 6.24 is studied. The numbering of the bodies of the system and their local coordinate frames are also pictured in Fig. 6.24. The double pendulum is made up of three rigid bodies, the ground body and two arms. One ideal revolute joint connects the two pendulum arms while a spatial revolute clearance joint, with a radial clearance size of 0.5 mm, exists between the ground and body 2. This simple multibody system is modeled with 18 coordinates and 11 kinematic constraints, which results in a system with 7 DOF.

Initially the double pendulum rests in the XZ plane position with pendulum arms perpendicular to each other. The system is then released from this initial configuration under gravity action only, which is taken as acting in the positive Y direction. The geometric dimensions and inertia properties of the double pendulum are listed in Table 6.3, while the dynamic parameters used in simulations are shown in Table 6.4.

In order to evaluate the influence of the spatial revolute clearance joint, in the dynamic performance of the double pendulum, the main kinematic and dynamic characteristics of the system response during the first 4 s of simulation are analyzed here, with the results compared to those obtained for a system with ideal joints. The

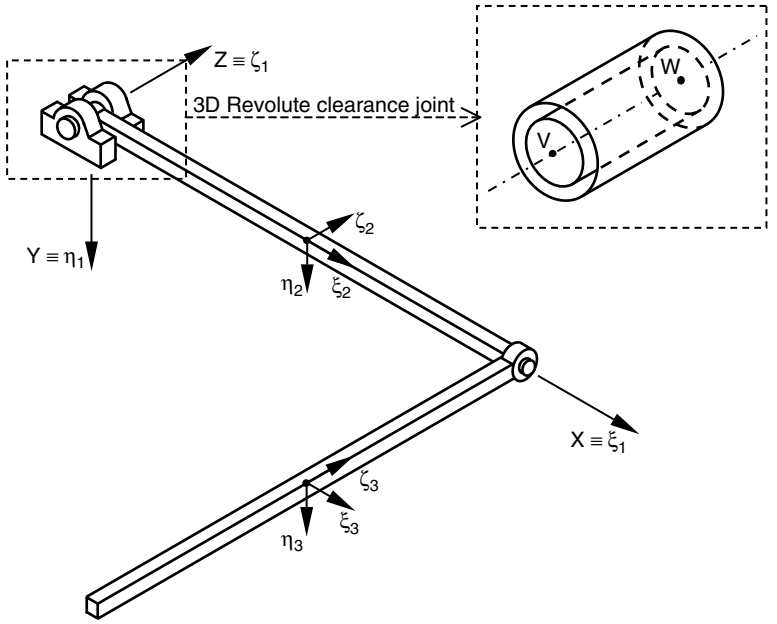

Fig. 6.24 Double pendulum modeled by two rigid bars and two revolute joints. Each bar is a prismatic homogeneous rigid body with square section of 0.03 m × 0.03 m

Table 6.3 Governing properties for the double pendulum

Body nr	Length (m)	Mass (kg)	Moment of inertia (Kg m^2)		
			$I_{\xi\xi}$	$I_{\eta\eta}$	$I_{\zeta\zeta}$
2	1.0	7.02	0.0010530	0.5855265	0.5855265
3	1.0	7.02	0.5855265	0.5855265	0.0010530

Hertz contact law with hysteresis damping factor, given by (3.9), is used to evaluate the contact forces caused by the impact in the clearance joint.

Figure 6.25a shows the normal contact force developed in the revolute clearance joint, during the first impact, and the reaction force of an ideal joint. The plotted reaction force is the module of the joint force in X direction developed at the ideal revolute joint that connects the two pendulum arms. In Fig. 6.25a, it is observed that the reaction force shape is similar to the shape of the contact force at the clearance joint. The maximum reaction force is about 50% of the contact force. Figure 6.25b shows the hysteresis curves for the first three impacts, developed at the clearance joint. As in the case of four-bar mechanism, analyzed in the previous section, the contact force decreases for each impact, suggesting that some of the system energy is dissipated from impact to impact. This dissipated energy is represented by the area enclosed by the hysteresis plot.

The position, velocity and acceleration of the center of mass of body 3 in the Y direction are plotted in Fig. 6.26a–c. Since the double pendulum has an open-loop topology, the existence of a clearance joint clearly influences the global position of the bodies of the system. The global behavior of the double pendulum with a clearance joint is characterized as nonlinear, almost chaotic, as illustrated in the Poincaré map of Fig. 6.26d. The velocity and acceleration components of the center of mass of body 3 in the Y direction are chosen to construct the Poincaré map. The complex densely filled appearance of the Poincaré map is an indicator that the system response is highly nonlinear.

The effect of the existence of a revolute clearance joint in the global motion of the double pendulum is illustrated in Fig. 6.27, in which the trajectory of the center of mass of the end arm is plotted during the first three seconds of simulation. The effect of the impacts, which occur at the clearance joint, produce very high peaks in the component of the reaction forces and moments used to represent the system response of the double pendulum, as it is shown in Fig. 6.28. Note that the reference quantities presented in Fig. 6.28, denoted as ideal joint, are obtained for the system model with ideal joints only.

Figure 6.29 shows the module of the eccentricity vector for both journal bases of the revolute clearance joint, as referred in Fig. 6.24. It can be observed that, for

Table 6.4 Simulation parameters for the double pendulum

Bearing radius	10.0 mm	Young's modulus	207 GPa
Journal radius	9.5 mm	Poisson's ratio	0.3
Radial clearance	0.5 mm	Integration step size	0.00001 s
Restitution coefficient	0.9	Integration tolerance	0.000001 s

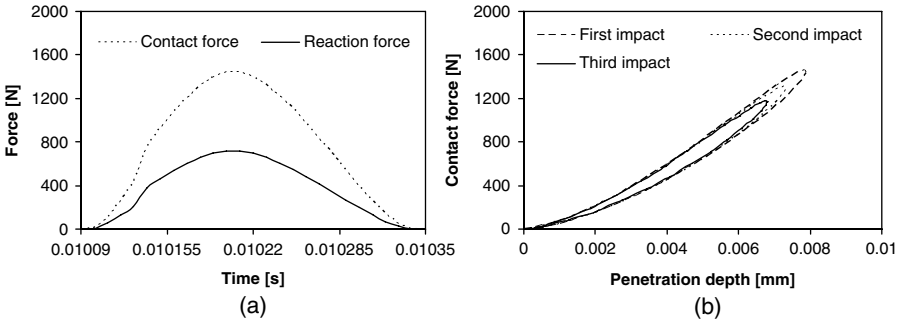

Fig. 6.25 (**a**) Normal contact force developed at the revolute clearance joint and reaction force in the ideal revolute joint that connects the two pendulum arms; (**b**) hysteresis loop of the first three impacts at the revolute clearance joint

the first impacts, the trajectories of the two bases are coincident. But, after that, the impacts between the journal and the bearing wall take place at different instants of time, meaning that some misalignment occurs. This phenomenon can be observed in Fig. 6.30 where a sequence of frames from a computer animation of the journal trajectory, relative to the bearing boundaries, is shown. The contact situations are represented by a dark journal, while the noncontact cases are represented by a light-colored journal. In the frame sequence the rebounds, during the first impacts, are

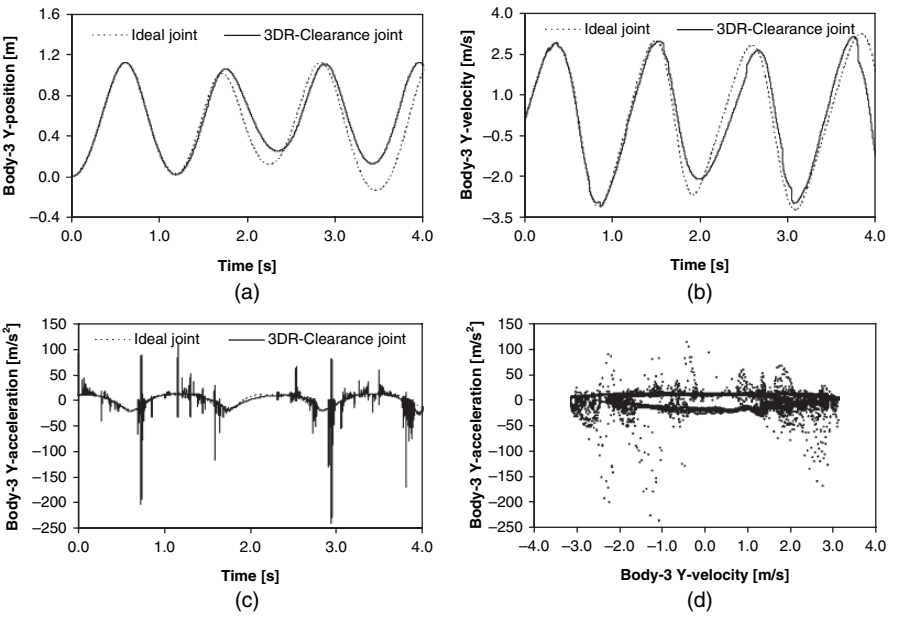

Fig. 6.26 (**a**) Y-position of body 3 center of mass; (**b**) Y-velocity of body 3 center of mass; (**c**) Y-acceleration of body 3 center of mass; (**d**) Poincaré map

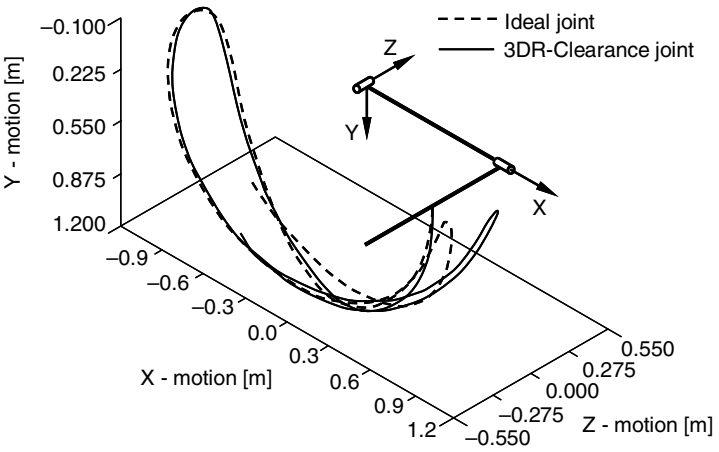

Fig. 6.27 Trajectory of the center of mass of the end arm during the first 3 s of simulation

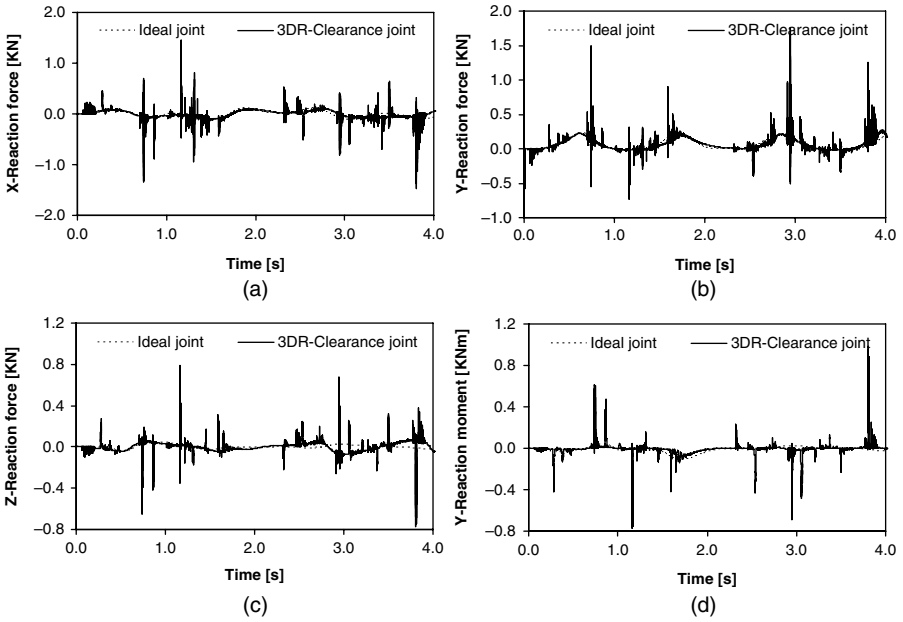

Fig. 6.28 Reaction forces and moment generated in the ideal joint: (**a**) X-reaction force; (**b**) Y-reaction force; (**c**) Z-reaction force; (**d**) Y-reaction moment

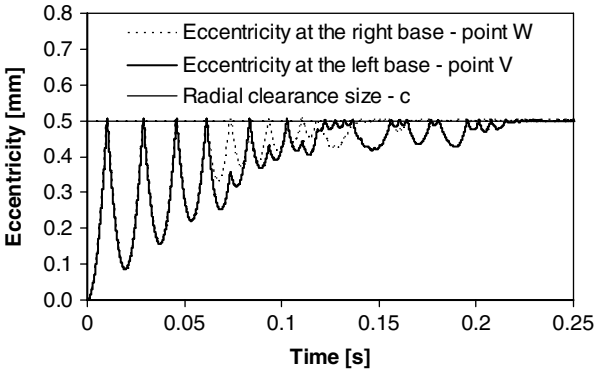

Fig. 6.29 Module of the eccentricity vector for the two journal bases of the revolute clearance joint

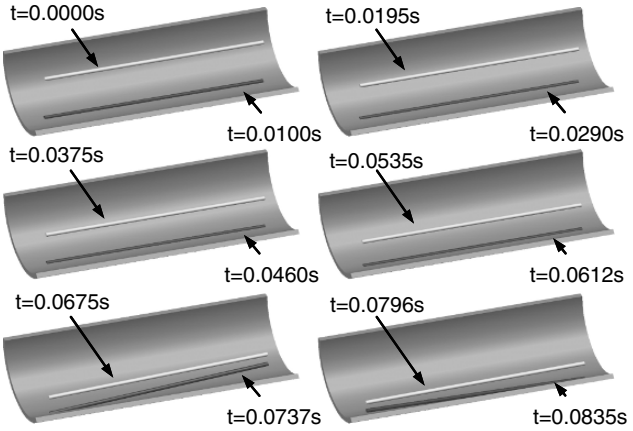

Fig. 6.30 Sequence of positions representing trajectory of the journal inside the bearing for first instants of simulation

clearly visible. Moreover the height of the rebound decreases from impact to impact due to the energy loss.

6.6 Demonstrative Example 3: Slider–Crank Mechanism

In this section, a spatial slider–crank mechanism is used as a numerical example to demonstrate the application of the methodologies previously presented. Four rigid bodies describe the slider–crank model under consideration. The model also includes one ideal revolute joint that connects the ground and the crank, one ideal spherical joint between the crank and the connecting rod and one ideal translational joint that connects the ground and the slider. A joint with clearance connects the slider to the connecting rod. This system has 19 independent kinematic constraints

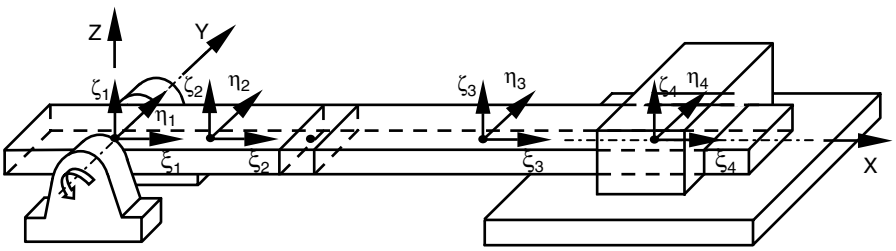

Fig. 6.31 Initial configuration of the spatial slider–crank mechanism with a clearance joint between the slider and the connecting rod

and it is described by 24 coordinates, which results in a mechanism with five degrees of freedom. A body-fixed coordinate system ($\xi\eta\zeta$) is attached to the center of mass of each body, and XYZ represents the global coordinate system. The slider–crank model shown in Fig. 6.31 is constrained to move in the XZ plane and therefore the overall motion described by the mechanism can be considered as planar. The gravitational acceleration is considered as acting in the negative Z direction.

The initial configuration is taken with the crank and the connecting rod collinear. The crank, which is the driving link, rotates about the Y-axis with a constant angular velocity of 150 rad/s. The crank velocity is maintained constant due to its very large rotational inertia, that is, the crank acts like a flywheel. The geometric characteristics and the mass and inertia properties are presented in Table 6.5.

The dynamic parameters used for the simulation are similar to those listed in Table 6.4. Furthermore the initial conditions necessary to start the dynamic analysis are obtained from kinematic simulation of a slider–crank model in which all the joints are considered to be ideal. In order to keep the analysis simple, all the joints are considered as frictionless.

In what follows, three different situations are analyzed. In the first one, the slider–crank mechanism is considered as a two-dimensional system and the joint between the connecting rod and slider is modeled as a 2D revolute clearance joint, as was presented in Chap. 4. In the second case, the slider–crank is modeled as a spatial multibody system and the clearance joint as a spherical joint with clearance, as developed in Sect. 6.2. Finally, in the third situation, the slider–crank is also considered as a spatial system and the joint clearance as a 3D revolute joint with clearance, as was presented in Sect. 6.3. For all three situations, the contacts between the elements

Table 6.5 Geometric and inertia properties for the dynamic simulation of the spatial slider–crank mechanism

Body nr	Length (m)	Mass (kg)	Moment of inertia (kg m^2)		
			$I_{\xi\xi}$	$I_{\eta\eta}$	$I_{\zeta\zeta}$
2	0.1524	0.15	10.0000	10.000	10.000
3	0.3048	0.30	0.0002	0.0002	0.0002
4	–	0.15	0.0001	0.0001	0.0001

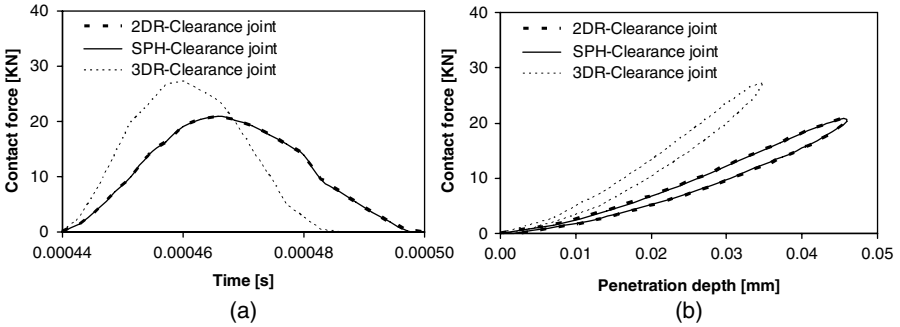

Fig. 6.32 (**a**) Normal contact force at the clearance joint for the different models; (**b**) hysteresis loop at the clearance joint. All the plots are for the first impact

that constitute the clearance joints are modeled by employing the Hertz contact law with hysteresis damping factor, expressed by mathematical equation (3.9).

The normal contact force developed at the clearance joint at the first impact, for the three different simulations, is plotted in Fig. 6.32a. Figure 6.32b shows the corresponding hysteresis curves. The contact force curves, obtained with 2D revolute clearance joint and with spherical clearance joint, coincide. This is expected

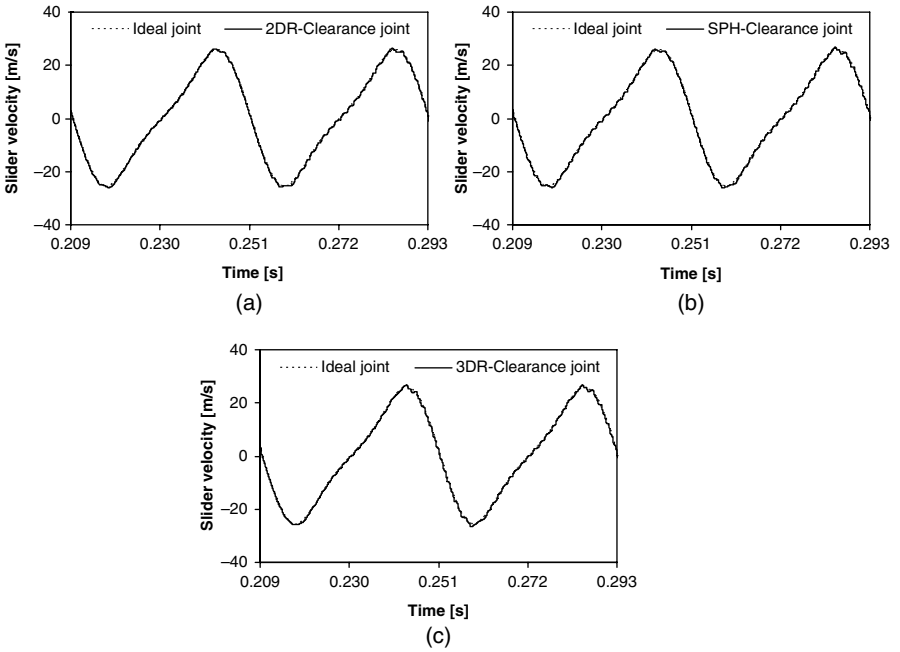

Fig. 6.33 Slider velocity for the different joint clearance models: (**a**) 2D revolute joint; (**b**) spherical joint; (**c**) 3D revolute joint

since the slider–crank model describes a planar motion and, therefore, the spherical clearance joint behavior can be considered equivalent to the case of the 2D revolute clearance joint. However, for the case of 3D revolute clearance joint simulation, the contact force curve presents a different evolution. Moreover the contact duration is shorter and the maximum force is greater than for the other two cases. This behavior can be understood due to the fact that in the 3D revolute model there are two point contacts, which are the two journal bases, instead of one point contact. Due to the nonlinear characteristics of the continuous force model, it is expected that representing the joint with one or two contact points leads to different results.

Figures 6.33 through 6.37 show the results for the case in which the radial clearance size is equal to 0.5 mm. In order to better understand the dynamic behavior of the slider–crank mechanism, these results are compared with those obtained for the ideal joint. The simulations are performed for the three different clearance joint models mentioned previously and at time interval corresponding to two complete crank rotations.

In Figs. 6.33 through 6.35, it is observed that the peaks on the slider acceleration curves are due to the contact force variation, which occurs during the period of contact between the elements that compose the clearance joints. The same phenomenon can be observed in the curves of the crank moment, because the contact forces are propagated through the rigid bodies of the slider–crank mechanism. It is noteworthy

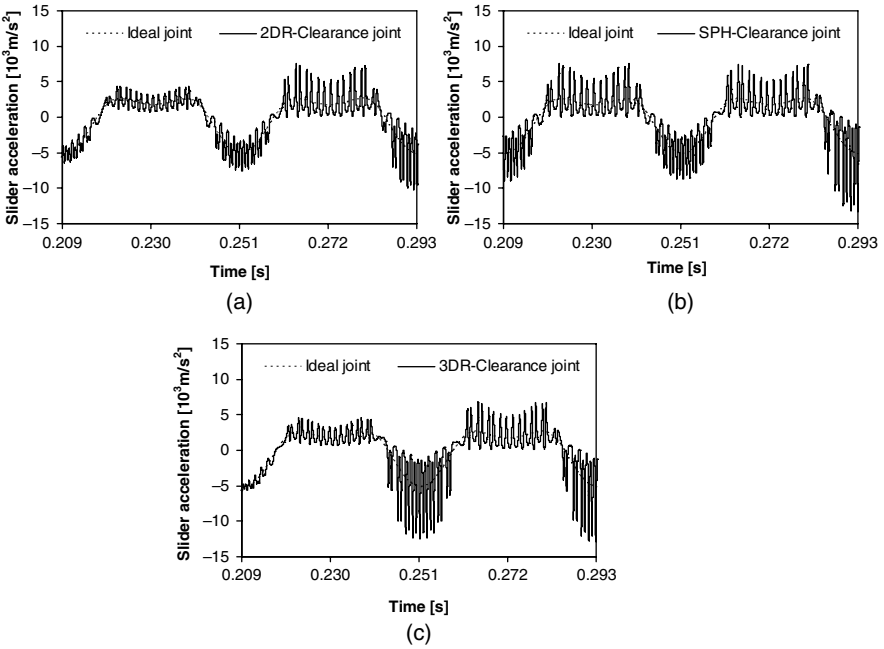

Fig. 6.34 Slider acceleration for the different joint clearance models: (**a**) 2D revolute joint; (**b**) spherical joint; (**c**) 3D revolute joint

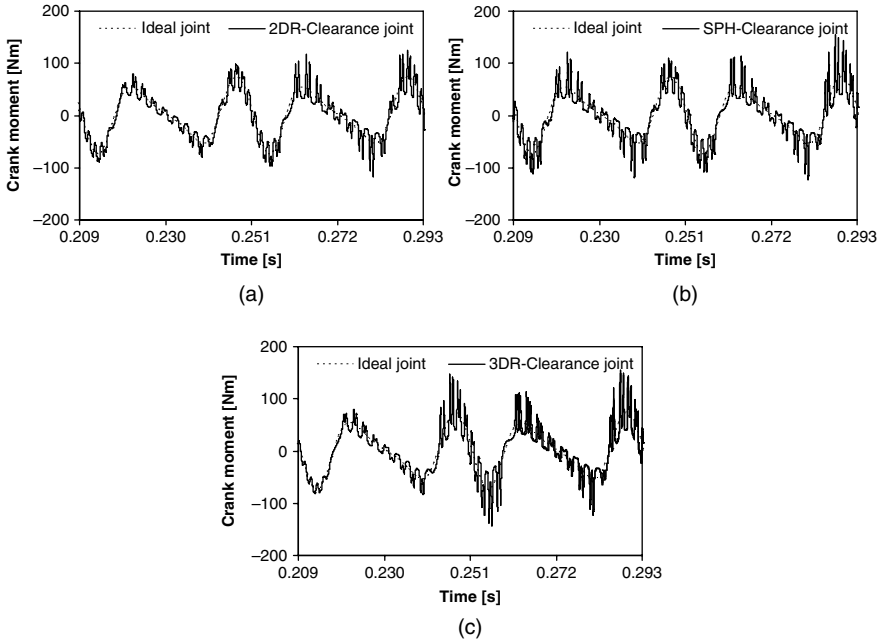

Fig. 6.35 Crank moment for the different joint clearance models: (**a**) 2D revolute joint; (**b**) spherical joint; (**c**) 3D revolute joint

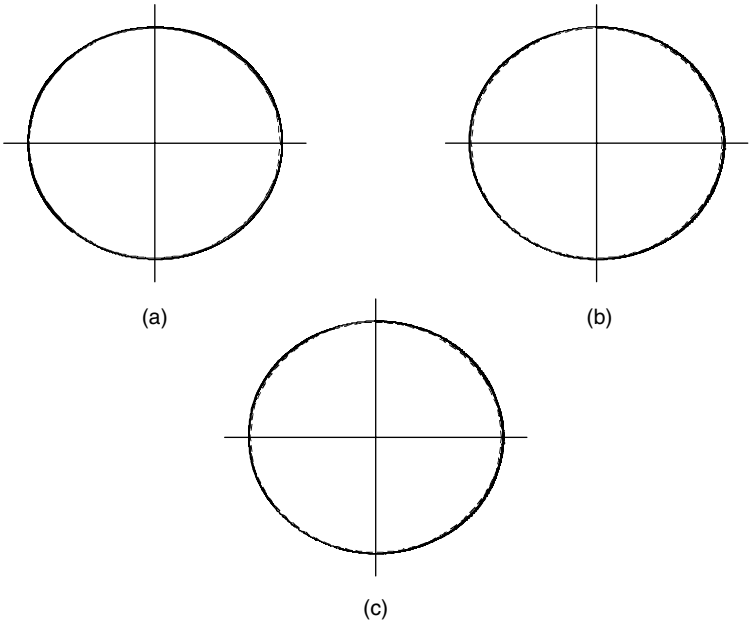

Fig. 6.36 Journal/ball motion inside the bearing/socket boundaries for different joint clearance models: (**a**) 2D revolute joint; (**b**) spherical joint; (**c**) 3D revolute joint

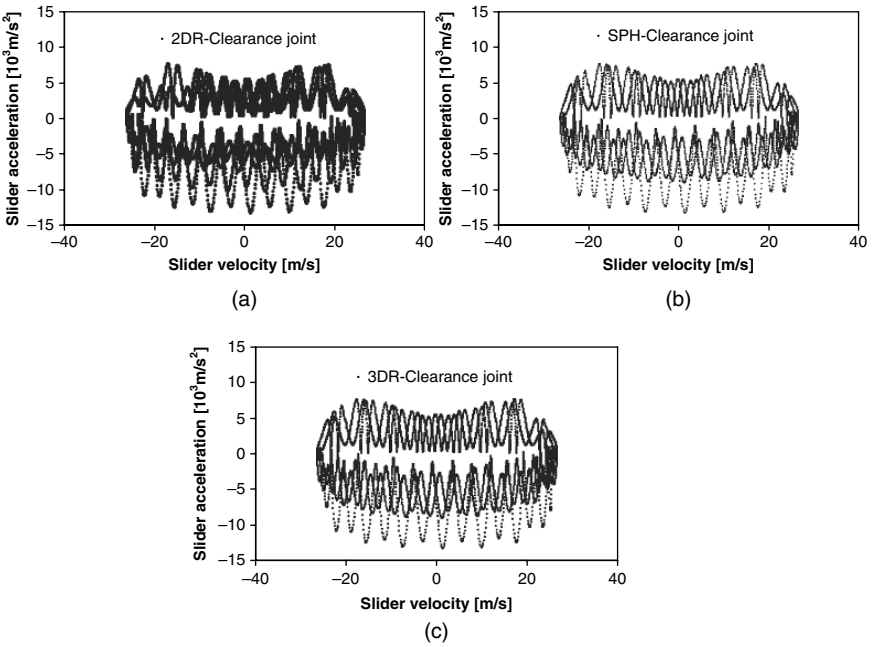

Fig. 6.37 Poincaré maps for the different joint clearance models: (**a**) 2D revolute joint; (**b**) spherical joint; (**c**) 3D revolute joint

that the global behavior of the slider–crank is the same for the three different clearance joint models, after the initial phase of the simulation. In fact, after $t=0.26$ s the magnitude of the moments is the same for all models. In the period prior to $t=0.26$ s, though the evolution of the crank moment is qualitatively the same, its magnitude differs for the different models. Figure 6.36 shows the relative motion between the journal and the bearing, and between the ball and the socket, for the three different joint clearance models. The dashed line represents the radial clearance size (0.5 mm). Since the slider–crank mechanism describes a planar trajectory, the relative motion between the journal and the bearing and between the ball and the socket occurs only in the plane XZ, the motion in the Y-direction being null. Therefore it is possible to compare the dynamic behavior of the 2D and 3D joint clearance formulations.

The dynamic response of the slider–crank mechanism is also represented by the evolution of velocity and acceleration of the slider and of the crank that acts on the crankshaft. Additionally the relative motion between the journal and the bearing, and between the ball and the socket centers, is plotted together with the corresponding Poincaré maps. The values of slider velocity and slider acceleration are plotted in the Poincaré maps in Fig. 6.37.

The Poincaré maps presented in Fig. 6.37 show that the global behavior of the slider–crank motion is nonlinear but tends to have a certain level of periodicity. Furthermore it is clear that both 2D and 3D models have a rather predictable motion,

their correlation, when measured by the outputs plotted in the Poincaré maps, being very high. The dynamic response of the spatial slider–crank mechanism with both spatial clearance joints, presented in this chapter, is consistent with the results obtained for the planar slider–crank model analyzed in Chap. 3, in which the two-dimensional revolute clearance joint modeling was used. This is expected, since the formulation for the spherical clearance joints is quite similar to that of the planar revolute clearance joints. Moreover the spatial slider–crank mechanism used in this section, apart from being a three-dimensional model, describes a planar motion due to the constrained topology.

6.7 Summary

In this chapter, a formulation for spatial dynamic analysis of multibody mechanical systems, employing the Cartesian coordinates and the Newton–Euler's approach, was presented. Euler parameters were used to define the angular orientation of bodies, which leads to a mathematical formulation without singularities. Additionally a simple and brief description of the standard mechanical joints of spatial multibody systems was presented. The constraint equations for the perfect spherical joint and for the perfect three-dimensional revolute joint were also presented in the first section of this chapter.

A general methodology for dynamic characterization of mechanical systems with spherical and three-dimensional revolute joints with clearance was formulated, for implementation in general-purpose computer codes. This formulation can be understood as an extension of that proposed for the two-dimensional multibody mechanical systems with clearance joints. The descriptions of spherical and three-dimensional clearance joints are based on the Cartesian coordinates, the joint elements are modeled as contact-impacting bodies and the dynamics of the joints is controlled by a continuous contact force model, which takes into account the geometric and mechanical characteristics of the contacting bodies. The normal force is evaluated as a function of the elastic pseudo-penetration depth between the impacting bodies, coupled with a nonlinear viscous-elastic factor representing the energy dissipation during the impact process. For this continuous contact force model, it is assumed that the compliance and damping coefficients are available.

Three illustrative examples and numerical results were presented, the efficiency of the developed methodologies being discussed in the process of their presentation. In order to keep the analysis simple, the friction and the lubrication effects were not included in the present chapter. However, the inclusion of these phenomena closely follows the procedures described in Chaps. 4 and 5.

A spatial four-bar mechanism was used with a spherical clearance joint formulation to demonstrate its application. The system was driven only by gravity, and the system was not conservative due to the presence of damping in the impact model, which leads to some energy dissipation in every cycle of the motion. This was observed by comparing the position and velocity of the mechanical system

with clearance to that of a system with ideal joints. Clearly the impacts within the clearance joint significantly increase the amount of dissipated energy.

In a second application, the double pendulum was used as a numerical example to illustrate the spatial revolute clearance joint formulation. In addition, a simple spatial slider–crank mechanism was used to study the influence of the clearance joint models in comparable planar and spatial mechanisms. A flywheel was incorporated in the crankshaft to maintain the crank angular velocity constant. It was observed that the overall results are consistent to those obtained for planar slider–crank model, that is, due to the clearance impacts the dynamic system presents much higher peaks in the acceleration time response and reaction forces than would be predicted if clearances were neglected. The system behavior clearly tends to be nonlinear and eventually chaotic, as shown by the corresponding Poincaré maps.

The overall results presented in this section show that the introduction of clearance joints in spatial multibody mechanical systems significantly influences the prediction of the components' position and drastically increases the peaks in acceleration and reaction moments at the joints. Moreover the system response clearly tends to be nonlinear when a clearance joint is included. This is a fundamental feature mainly in high-speed and precision mechanisms where the accurate predictions are essential for the design of the mechanical systems.

References

Baumgarte J (1972) Stabilization of constraints and integrals of motion in dynamical systems. Computer Methods in Applied Mechanics and Engineering 1:1–16.

Haug EJ (1989) Computer-aided kinematics and dynamics of mechanical systems. Vol. I: basic methods. Allyn and Bacon, Boston, MA.

Lankarani HM, Nikravesh PE (1990) A contact force model with hysteresis damping for impact analysis of multibody systems. Journal of Mechanical Design 112:369–376.

Nikravesh PE (1988) Computer-aided analysis of mechanical systems. Prentice Hall, Englewood Cliffs, NJ.

Nikravesh PE, Chung IS (1982) Application of Euler parameters to the analysis of three-dimensional constrained mechanical systems. Journal of Mechanical Design 104:785–791.